Simulation of nonadiabatic processes on surfaces

Christian Bach

Technische Universität München
Physik-Department T30
Univ.-Prof. Dr. A. Groß

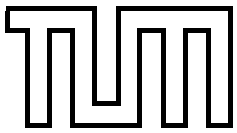

Simulation of nonadiabatic processes on surfaces

Christian Bach

Vollständiger Abdruck der von der Fakultät für Physik der Technischen Universität München zur Erlangung des akademischen Grades eines

Doktors der Naturwissenschaften (Dr. rer. nat.)

genehmigten Dissertation.

Vorsitzende:		Univ.-Prof. Dr. K. Krischer
Prüfer der Dissertation:	1.	Univ.-Prof. Dr. A. Groß
	2.	Univ.-Prof. Dr. W. Brenig, em.

Die Dissertation wurde am 23. März 2004 bei der Technischen Universität München eingereicht und durch die Fakultät für Physik am 14. Juni 2004 angenommen.

Abstract

A simple one dimensional two state model for the laser induced desorption and the desorption of NO from a NiO(100) surface are investigated. This is done by utilising a mixed quantum classical algorithm derived from generalised surface hopping [1]. The algorithm used is a surface hopping method with optical potentials describing the electronic excitation and de-excitation processes. The simple model is used to explore the dependence of the desorption probability on the potential parameters. We show that the critical parameters are the lifetime, the separation of the minima and the width of the excited state potential.

For the NO/ NiO(100) system the electronic states taken into account are the ground state and one charge transfer state. The corresponding forces used in the dynamic simulation are based on two dimensional ab initio potentials, calculated by Klüner et al. [2]. These were extended by simple models to a full description of the desorbing molecule together with one surface coordinate. In the simulations two species of desorbing molecules are found, one with early and the other with late desorption times. The second species accounts for most of the difference in desorption yield found when comparing the mixed quantum classical simulation to the wave packet results in [3]. When investigating the effect of additional degrees of freedom on the dynamics we find the surface oscillator to be the most decisive one, slowing down the early desorbing molecules and lowering the rotational temperature of the desorbed molecules substantially.

Zusammenfassung

Durch Simulation mit einem gemischt quanten-klassischen Algorithmus wird die laserinduzierte Desorption von Molekülen von einer Festkörperoberfläche untersucht. Im ersten Teil der Arbeit wird ein einfaches eindimensionales zwei Zustände Modell betrachtet und die Abhängigkeit der Desorptionswahrscheinlickeit von den verschiedenen Modellparametern untersucht. Der zweite Teil ist der Desorption von NO von einer NiO(100) Oberfläche gewidmet. Ausgehend von zweidimensionalen ab initio Potentialen von T. Klüner et al. für den Grundzustand und einen Elektronentransferzustand erweitern wir das Modell auf sämtliche Molekülfreiheitsgrade und führen zusätzlich einen Oberflächenoszillator ein. Der Einfluss der einzelnen Freiheitsgrade auf die Desorptionsdynamik wird untersucht und es zeigt sich, dass die Hinzunahme des Oberflächenfreiheitsgrades den größten Einfluss hat.

Acknowledgements

First of all I would like to thank my supervisor Prof. Dr. Axel Groß for giving me the chance to pursue my PhD in the exciting field of surface science. I am grateful for his invaluable support and the many things he taught me about the physics of surfaces.

I am also in debt to present and former members of the T30g and the T32 group, Areezo Dianat, Dr. Moritz Hilf, Dr. Markus Lischka, Thomas Markert, Christian Mosch, Ata Roudgar, Sung Sakong and Prof. Dr. Wilhelm Brenig for constant support and many interesting discussions, not all about physics.

For making life at the physics department a lot easier I want to thank Mrs. Liebhart-Schilling and Mrs. Sprzagala. Many thanks also go to Dr. Herbert Müller for his support in all computer matters.

Many thanks go to the members of the Schwerpunkt Programm 1093 of the Deutsche Forschungsgemeinschaft, especially Dr. Thorsten Klüner for providing me with the ab initio potentials and the results of his wave packet simulations and to Prof. Dr. Helmut Zacharias for the coordination of the Schwerpunkt and interesting discussions about the NO/NiO system.

I would like to thank the Wilhelm und Else Heraeus-Stiftung for providing me with financial support for attending the DPG-Frühjahrstagungen in 2001, 2002 and 2003. Most of the support was provide by the Deutsche Forschungsgemeinschaft via the Schwerpunkt Programm 1093, Dynamik von Elektronentransferprozessen an Grenzflächen.

I especially want to thank my parents and my brother for constant support and encouragement during the past years.

München Christian Bach
March 2004

Contents

List of Figures

List of Tables

Chapter 1

Introduction

Desorption of molecules from surfaces induced by electronic transitions (DIET), triggered either by photons or electrons, has been studied extensively in the last decades [4–6]. In recent years, technological progress made it possible to perform time-resolved laser pump-probe experiments in which the time evolution of DIET processes can be monitored in the femtosecond regime [7, 8]. These experiments provide a wealth of information on the real-time dynamics of chemical processes at surfaces [9, 10].

Unfortunately the development of theoretical tools for the realistic description of DIET processes did not match the experimental progress. The main reason for this is the fact that the modelling of processes involving several electronic states and transitions between them still represents a great challenge. First of all, for the ab initio determination of excited state potentials it is not possible to use the computational efficient density-functional theory schemes, which work so well for the ground state. Instead one has to rely on quantum chemistry methods which are usually computational very costly. And second, the simulation of the dynamics of DIET processes explicitly requires the simultaneous treatment of both the electronic and the nuclear dynamics. There has been significant progress in the high-dimensional simulation of Born-Oppenheimer reaction dynamics at surfaces in recent years [11–15]. These studies in fact demonstrated the importance of the multidimensionality in the reaction dynamics. However, electronically nonadiabatic simulations of reactions at surfaces are usually limited to a few degrees of freedom [16]. This is caused by the difficulties in the theoretical treatment due to the different time scales relevant for the electronic and nuclear motion.

To allow a multidimensional treatment of laser-induced desorption, we propose the use of mixed quantum-classical schemes in which the nuclear motion is described classically while at the same time the electrons are treated quantum mechanically. Still the feedback between quantum and classical degrees of freedom has to be taken into account in a self-consistent way. We already implemented such a scheme for the description of charge transfer processes in the scattering of iodine molecules at a

diamond surface [17, 18]. The mixed quantum-classical scheme we will use is based on the fewest switches algorithm developed by Tully [19]. This surface-hopping algorithm minimises the number of state switches under the constraint of maintaining the correct statistical population of each electronic state, as given by the quantum mechanical part of the system. In order to include th e effect of substrate states, we will extend this algorithm by including an optical potential.

The aim of this work is to investigate the usefulness of mixed quantum classical algorithms for the simulation of the dynamics of nonadiabatic reactions, i.e. processes involving more than one electronic state. The processes we will discuss explicitly all belong to the class of laser induced desorption of simple molecules from surfaces.

In the following chapter we first discuss our model of DIET processes and some mixed quantum classical methods to describe such reactions. In the third chapter we investigate a simple one dimensional two-state model inspired by experiments to the desorption of NO molecules from small Pd-cluster [20]. After that we will discuss a more detailed model of the laser induced desorption of NO from a nickel-oxide surface. In chapter 5, we then will summarise our results.

Chapter 2

Theory of Nonadiabatic Reactions

The aim of this work is to model the dynamics of nonadiabatic processes at surfaces. More precisely we want to study reactions proceeding not only in the electronic ground state but also in excited states. As our main application we will discuss laser induced desorption of NO molecules from a single-crystal nickel oxide (100) surface and small palladium clusters on alumina support. The desorption from Pd-clusters gives motivation for simple model calculations in one dimension while the NO/NiO system will be treated in a more complex model based on two dimensional ab initio potential energy surfaces calculated by T. Klüner et al. [2].

Both reactions belong to the larger class of desorption induced by (multiple) electronic transitions (DI(M)ET). These are reactions where the desorption of a molecule initially adsorbed on a surface is triggered by one or more electronic excitations. Usually these excitations are initiated by light irradiation or electron beams. While in the excited state, the adsorbate is exposed to forces different from the ground state and will start to move. After relaxation back into the ground state the molecules may or may not desorb. In principle the dynamics of such reactions is given by the Schrödinger equation. Relativistic effects can usually be neglected in the description of chemical reactions, however they play a role in calculating the electronic core levels of all but the lightest atoms and must be taken into account in total energy calculations. Since finding a solution of the Schrödinger equation for the complete system is intractable the general strategy is to split the system into two parts, one with the light and thus fast moving electrons and the other part consisting of the nuclei. The electronic subsystem must be treated quantum mechanically but the nuclei might be treated classically. How and to what degree the interaction between the two parts is taken into account distinguishes different methods. One possible way of accounting for the coupling between the electronic and the nuclear part is surface hopping, where the time evolution of the slow coordinates is given by only one electronic state at any time in contrast to mean field where an average over all electronic states is used.

Quantum mechanical solutions for the nuclear system can be obtained by either

solving the time dependent equations with wave packet methods [3, 21] or for example the coupled channel method resulting in time independent solutions [11, 22, 23]. So far this can be done for up to six or seven nuclear degrees of freedom [13, 15] depending on the details of the simulation. But the scaling of the time and memory necessary to perform such simulations is rather unfavourable and including further coordinates would require either much faster computers and improved algorithms. If classical mechanics is used it is possible to include a large number of degrees of freedom and to propagate for long simulation times. But there are also problems in using classical mechanics. For example in order to obtain statistical significant results one needs to sample over a large number of trajectories.

The ground state of the electronic system for a fixed set of nuclear coordinates can be found efficiently using density functional theory [24, 25]. This can be done for rather large systems, also giving the ground state forces on the nuclei. Since we are interested in reactions explicitly involving excited states we also need the corresponding excited state potential energy surfaces. Unfortunately these are much harder to calculate. The focus of this work is modelling the dynamics of molecules desorbing from surfaces by laser irradiation and thus we will not discuss further how to calculate the potential energy surfaces and the couplings between the different electronic states, which are needed as input for our simulations. The calculation of the potentials is by no means easy especially for the excited electronic states and the couplings. We will also not discuss how to derive analytical expressions for the potential energy surfaces from the calculated energies, since the whole problem of fitting in high dimensions is a field of research for its own [26].

In the following sections we will first present our model for the description of DI(M)ET processes. After that we will discuss some methods for the solution of our model of nonadiabatic reactions.

2.1 Model

Usually desorption processes induced by electronic transitions are described in one dimension either within the Menzel-Gomer-Redhead (MGR) model [27, 28] or the Antoniewicz model [29]. These models involve two electronic states the ground and an excited state in which the nuclei move. The initial excitation is taken into account as a Frank-Condon transition, i.e. position and velocity remain unchanged during the excitation. This is also referred to as the sudden approximation. The initial transition is followed by a propagation of the adsorbate in the excited state for a certain time, the residence time, after which another Frank-Condon transition transfers the system back into the ground state. The MGR and the Antoniewicz model differ by their relative position of the excited state potential minimum with respect to the ground state potential minimum. The sole coordinate in these models is the reaction path coordinate. This is the coordinate along the minimum path in the potential energy surface of the nuclear coordinates connecting the reactants with the products. In our case the reactants are the adsorbate bound to the surface and the products are the surface together with the adsorbate far away from the surface. In the MGR model the

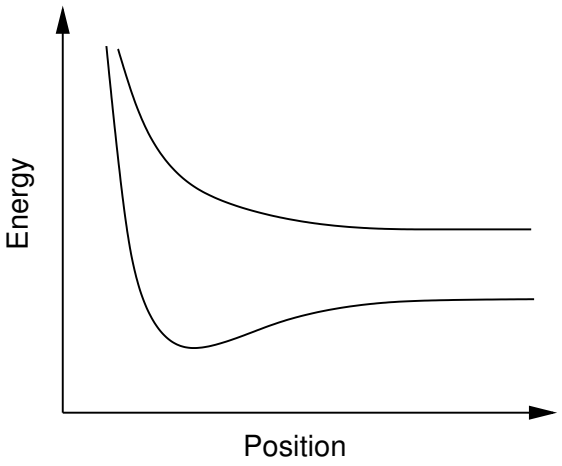

Figure 2.1: Energy diagram for the Menzel-Gomer-Redhead model.

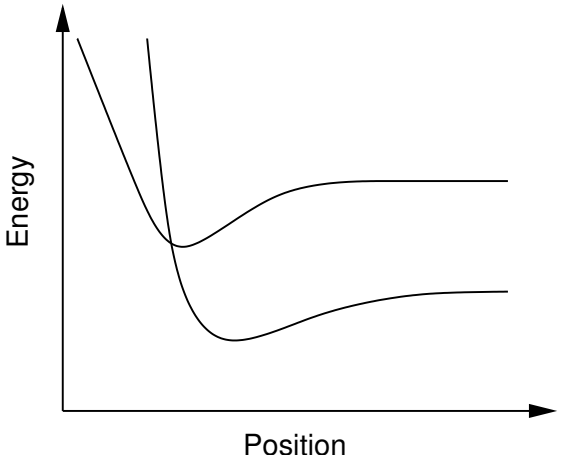

Figure 2.2: The potential energy surfaces for the Antoniewicz model.

excited state minimum is further away from the surface (see figure 2.1) and the excited state might even be repulsive. Thus upon excitation the adsorbate is accelerated away from the surface and if the lifetime is long enough it gains enough kinetic energy to desorb after the relaxation back into the ground state.

In the Antoniewicz model the excited state is a bound state with the minimum closer to the surface (figure 2.2). This is the typical situation for electron transfer states where the adsorbate becomes partially ionised and due to image charge forces is attracted towards the surface, as it is the case for the NO on nickel oxide system we will discuss later. After a Frank-Condon transition into the excited state the adsorbate molecule is accelerated towards the surface and after relaxation hits the repulsive wall of the ground state and possibly desorbs from there.

Both models allow an estimation of the isotope effect on the desorption probability [30]. For short lifetimes in the excited state and thus only small distances travelled, the force F accelerating the adsorbate and the lifetime τ can be assumed to be inde-

pendent of the reaction path coordinate z. All molecules in the excited state reaching a certain critical distance from the surface z_c at which point they gained enough kinetic energy to overcome the desorption barrier will desorb. The time t_c required to reach that distance, with constant acceleration, is

$$t_c = \sqrt{\frac{2\,|z_c - z_0|}{F}\, m} = c\sqrt{m}, \tag{2.1}$$

where z_0 is the position where the Frank-Condon transition takes place and m is the mass of the adsorbate. The constant $c = \sqrt{\frac{2|z_c - z_0|}{F}}$ should be the same for different isotopes of the adsorbate. Thus the escape probability for an excited adsorbate is

$$P = e^{-\frac{t_c}{\tau}} = e^{-\frac{c\sqrt{m}}{\tau}}, \tag{2.2}$$

where we made use of the assumption, that the lifetime in the excited state is independent of the position. Since we would expect the excitation probability to be equal for all isotopes of the adsorbate the ratio of the desorption cross-sections σ is given by the ratio of the escape probabilities

$$\frac{\sigma_1}{\sigma_2} = \frac{P_1}{P_2} = \frac{e^{-\frac{c\sqrt{m_1}}{\tau}}}{e^{-\frac{c\sqrt{m_2}}{\tau}}} = P_1^{\left(1-\sqrt{\frac{m_2}{m_1}}\right)}, \tag{2.3}$$

where the index $i = 1, 2$ denotes the different isotopes.

In contrast to gas phase reactions there are in general a lot more than just two electronic states in an adsorbate substrate system. These can be split into a set of adsorbate levels together with substrate excitations, compare [31]. Figure 2.3 shows a schematic drawing of two such adsorbate states, labelled G for the adsorbate ground state and A for an adsorbate excitation and their shifts due to electronic excitations of the substrate. It also sketches the variation of those levels with the nuclear reaction path coordinate. In that picture the desorption of the adsorbate through an electronic excitation, either with light or an electron beam, can be split into five steps depicted by the arrows and dots in figure 2.3.

First the system is electronically excited, this might be direct into an excited adsorbate state or indirect via the creation of hot electrons in the substrate (step 1) followed by a Frank-Condon transition into the adsorbate state A (step 2), for example by the transfer of one electron from the substrate to the adsorbate. Since in general the minimum energy position of the ground and excited state differ the adsorbate is accelerated in the excited state (3). After a certain period of time the adsorbate returns to the electronic ground state with the excess energy being transfered to electronic excitations of the substrate (4). If the adsorbate gained enough energy to overcome the desorption barrier it will eventually desorb (5). More exactly, in order for an desorption event to occur the energy in the reaction path coordinate must be larger than the binding energy. If the energy transfer between different degrees of freedom is slow the adsorbate might be trapped dynamically in front of the surface for a very long time, despite a positive total energy [32, 33].

Another point is the fact that the adsorbate might become excited more than just once. Such a process would then be termed desorption induced by multiple electronic

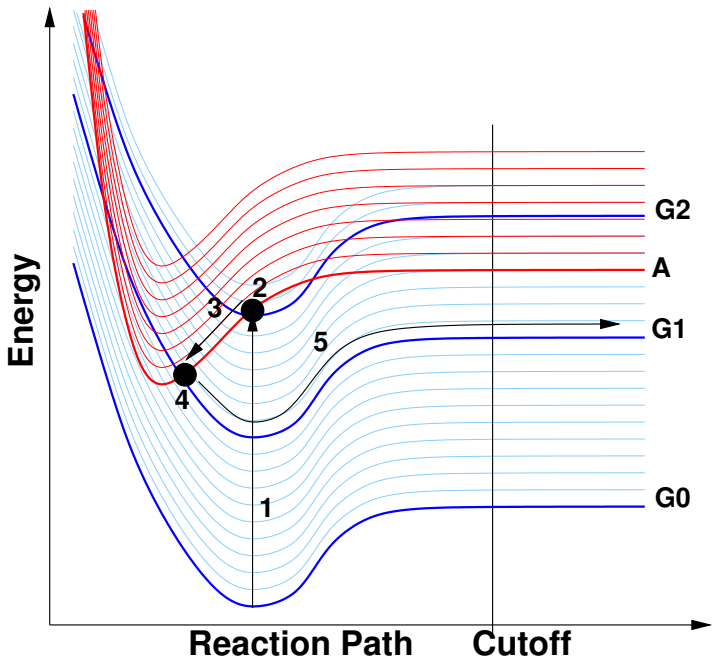

Figure 2.3: Schematic drawing of a DIET process. The potential curves labelled G0–G2 correspond to the adsorbate ground state with different substrate excitations, while the curve labelled A corresponds to an excitation of the adsorbate. Thin dashed lines represent the adsorbate ground state together with the not explicitly involved substrate states. The numbers 1–5 indicate the five steps of the desorption process.

excitations. Such reactions can be split into two classes depending on whether the second excitation takes place while the adsorbate is still in the excited state or already relaxed back into the ground state. Due to the correlated excitations in the first type of DIMET, such processes are characterised by an exponential dependence of the desorption yield on the excitation intensity, in contrast to the linear dependence observed in single excitation processes. DIMET can be important for excitations via ultra short laser pulses where the energy density of the pulse is usually higher than in longer pulses or constant wave mode.

In order to simulate the dynamics of such processes all relevant nuclear coordinates, electronic states and the coupling between those states have to be taken into account. Since we are interested in processes explicitly including excited states the Born-Oppenheimer approximation can not be employed. But still a first step, when dealing with such complex systems with different time scales relevant for different degrees of freedom, is a separation between slow, denoted by r, and fast, denoted by R, moving coordinates. The fast degrees of freedom, usually the electrons, will require explicit quantum mechanical treatment. The dynamics of the slow coordinates can be treated with quantum mechanical methods but in most cases a classical treatment will

be sufficient. We will use the term electronic coordinates as a synonym for the fast degrees of freedom, despite the fact that those might include some proton positions as well [34, 35]. Correspondingly we will use the term nuclear coordinates for the slow degrees of freedom. In the next sections we will discuss the theoretical treatment of such systems, following mainly the discussion of Tully in references [36, 37].

The Hamilton operator of a system that separates into slow and fast degrees of freedom can be written in the following form

$$H(r, R) = T_R + T_r + V(r, R), \tag{2.4}$$

where V is the potential and T_R and T_r are the kinetic energy operators for the slow degrees of freedom and respectively for the electronic coordinates. The potential can be split further into three parts

$$V(r, R) = V_{rr}(r) + V_{RR}(R) + V_{rR}(r, R), \tag{2.5}$$

the interaction of the electrons with each other $V_{rr}(r)$ the interaction between the nuclei $V_{RR}(R)$ and the interaction of the nuclei with the electrons $V_{rR}(r, R)$. Likewise the kinetic energy operators can be specified further, for the nuclear operator we have

$$T_R = -\sum_{\alpha=1}^{3N} \frac{\hbar^2}{2M_\alpha} \frac{d^2}{dR_\alpha^2} \tag{2.6}$$

where N is the number of nuclei and M_α the mass corresponding to the α-th coordinate R_α. Similar for the electrons we get

$$T_r = \frac{-\hbar^2}{2m_e} \sum_{\beta=1}^{3n} \frac{d^2}{dr_\beta^2} \tag{2.7}$$

where now n is the number of electrons in the system and m_e is the electron mass and r_β the β-th electronic coordinate. For simplicity we use Cartesian coordinates throughout our theoretical discussion, but other coordinates could also be used. If light nuclei are to be included in the fast moving coordinates the mass can not be pulled out from under the sum and T_r is given by a formula similar to (2.6). We sometimes will use $T_R = \frac{-\hbar^2}{2M}\nabla_R^2$ and $T_r = \frac{-\hbar^2}{2m}\nabla_r^2$ as an abbreviation to (2.6) and (2.7) respectively.

The dynamics of the system is given by the solution of the time dependent Schrödinger equation

$$i\hbar \frac{\partial}{\partial t} \Psi(r, R, t) = H\Psi(r, R, t). \tag{2.8}$$

The wave function $\Psi(r, R, t)$ of the whole system can be written in two ways, either as an product expansion with a nuclear $\psi(R, t)$ and an electronic part $\phi(r, t)$

$$\Psi(r, R, t) = \psi(R, t)\phi(r, t) \tag{2.9}$$

or as an expansion in eigenfunctions $\phi_i(r, R)$ of an electronic Hamiltonian and time dependent coefficients $\psi(R, t)$

$$\Psi(r, R, t) = \sum_i \psi_i(R, t)\phi_i(r, R). \tag{2.10}$$

The first ansatz leads to the mean field approximation and the second one to surface hopping as we will show in the following sections.

2.2 Mean Field Approximation

As mentioned before the mean field approximation is base on a product expansion of the wave function

$$\Psi(r,R,t) = \psi(R,t)\phi(r,t)e^{\frac{i}{\hbar}\gamma(t)}, \tag{2.11}$$

where we, in contrast to (2.9), introduced an additional phase γ which will be specified later [36, 38]. The normalisation condition for the total wave function

$$\int dR\, dr\; \Psi^\star(r,R,t)\Psi(r,R,t) = 1 \tag{2.12}$$

is satisfied by requiring $\gamma(t)$ to be real valued and by independent normalisation conditions for $\psi(R,t)$ and $\phi(r,t)$.

$$\int dr\; \phi^\star(r,t)\phi(r,t) = 1 \tag{2.13}$$

$$\int dR\; \psi^\star(R,t)\psi(R,t) = 1 \tag{2.14}$$

If we insert equation (2.11) into equation (2.8), multiply by $\psi^\star(R,t)$ from the left and integrate over the whole space of nuclear coordinates R we get

$$i\hbar\frac{\partial\phi}{\partial t} = \left[T_r + V_{rr} + \dot\gamma + \int dR\; \psi^\star\left(-i\hbar\frac{\partial}{\partial t} + T_R + V_{RR} + V_{rR}\right)\psi\right]\phi \tag{2.15}$$

and similar for ψ with multiplication of $\phi^\star$ and integration over r

$$i\hbar\frac{\partial\psi}{\partial t} = \left[T_R + V_{RR} + \dot\gamma + \int dr\; \phi^\star\left(-i\hbar\frac{\partial}{\partial t} + T_r + V_{rr} + V_{rR}\right)\phi\right]\psi. \tag{2.16}$$

In equations (2.15) and (2.16) the action of one part of the system onto the other is given in an integral way and thus averaged over the whole space, hence the name mean field. Another feature of these equations is that they are independent of the basis set used to construct the wave functions ψ and ϕ.

We still have to specify γ. To do so we multiply equation (2.15) by $\phi^\star$ and integrate over R. This results in an additional equation containing $\dot\gamma$

$$i\hbar\int dR\; \psi^\star\frac{\partial\psi}{\partial t} + i\hbar\int dr\; \phi^\star\frac{\partial\phi}{\partial t} - \dot\gamma = \tag{2.17}$$

$$\int dr\; dR\; \psi^\star\phi^\star\left[T_r + T_R + V_{rr} + V_{RR} + V_{rR}\right]\phi\psi = E$$

with the total energy of the system E. The same equation can be derived from (2.16) by multiplication with $\psi^\star$ and integration over r. Equation (2.17) together with energy conservation imposes a constraint on the phase γ and the integrals $\int dR\; \psi^\star\frac{\partial\psi}{\partial t}$ and

$\int dr\ \phi^\star \frac{\partial \phi}{\partial t}$ which can be defined arbitrarily otherwise. A suitable choice, as will be clear later when taking the classical limit for the slow degrees of freedom, is the following:

$$\gamma = \int^t d\tau\ E_r(\tau), \tag{2.18}$$

$$i\hbar \int dr\ \phi^\star \frac{\partial \phi}{\partial t} = E_r(t) \tag{2.19}$$

and

$$i\hbar \int dR\ \psi^\star \frac{\partial \psi}{\partial t} = E, \tag{2.20}$$

where we introduced the electronic Hamiltonian $H_r(r, R)$

$$H_r(r, R) = T_r + V_{rr}(r) + V_{rR}(r, R). \tag{2.21}$$

The corresponding expectation value is

$$E_r(t) = \int dr\ dR\ \psi^\star(R, t)\phi^\star(r, t)H_r(r, R)\phi(r, t)\psi(R, t), \tag{2.22}$$

which is real valued, as the expectation value of the Hermitian operator H_r and thus γ is also real valued as required for the normalisation condition. Inserting this into equations (2.15) and (2.16) we get a new set of coupled equations

$$i\hbar \frac{\partial \phi(r, t)}{\partial t} = \left[T_r + V_{rr}(r) + \int dR\ \psi^\star(R, t)V_{rR}(r, R)\psi(R, t) \right] \phi(r, t) \tag{2.23}$$

and

$$i\hbar \frac{\partial \psi(R, t)}{\partial t} = \left[T_R + V_{RR}(R) + \int dr\ \phi^\star(r, t)H_r(r, R)\phi(r, t) \right] \psi(R, t). \tag{2.24}$$

Now the integral in equation (2.23) does no longer contain terms involving derivatives, which will allow us in the classical limit to replace the nuclear wave function by a delta function.

2.2.1 Classical Limit

From these equations it is now possible to derive a classical limit for the slow coordinates. The procedure we use is similar to the one used by Bohm [39]. We start by spliting the slow wave function $\phi(R, t)$ into amplitude and phase

$$\psi(R, t) = A(R, t)e^{\frac{i}{\hbar}S(R,t)} \tag{2.25}$$

with $A(R, t)$ and $S(R, t)$ being real valued functions. Inserting this into equation (2.24) and spliting into real and imaginary part we get

$$-A\dot{S} = -\frac{\hbar^2}{2M}\nabla_R^2 A + \frac{A}{2M}\left(\nabla_R S\right)^2 + V_{RR}A + \left[\int dr\ \phi^\star(r, t)H_r(r, R)\phi(r, t) \right] A \tag{2.26}$$

and

$$\dot{A} = -\frac{1}{M}\left(\nabla_R A\right)\left(\nabla_R S\right) - \frac{1}{2M} A\left(\nabla_R^2 S\right). \tag{2.27}$$

Division by $-A$ and some rearrangement of (2.26) lead to

$$\dot{S} + \frac{1}{2M}\left(\nabla_R S\right)^2 + V_{RR} + \left[\int dr\ \phi^\star(r,t) H_r(r,R)\phi(r,t)\right] = \frac{\hbar^2}{2M}\frac{\nabla_R^2 A}{A}. \tag{2.28}$$

The equations (2.28) and (2.27) are equivalent to the original equation (2.24), note that equation (2.27) does not contain $\hbar$. Now we can take the classical limit $\hbar \to 0$ of (2.28), i.e. we neglect the term on the righthand side and get

$$\dot{S} + \frac{1}{2M}\left(\nabla_R S\right)^2 + V_{RR} + \left[\int dr\ \phi^\star(r,t) H_r(r,R)\phi(r,t)\right] = 0. \tag{2.29}$$

This is the classical Hamilton-Jacobi equation

$$H\left(R, \frac{\partial S}{\partial R}\right) + \frac{\partial S}{\partial t} = 0 \tag{2.30}$$

with Hamilton function

$$H(R,P) = \frac{1}{2M}P^2 + V_R^{MF}(R) + V_{RR}(R). \tag{2.31}$$

with the mean field potential $V_R^{MF}(R)$ containing the action of the fast wave function on the slow coordinates, being defined as

$$V_R^{MF}(R) = \int dr\ \phi^\star(r,t) H_r(r,R)\phi(r,t). \tag{2.32}$$

S is the classical action

$$S\left\{R(t)\right\} = \int^t L(R, \dot{R}, \tau) d\tau \tag{2.33}$$

with L being the Lagrange function and the derivative of S with respect to the nuclear coordinates gives the corresponding conjugate momentum

$$P_\alpha = \frac{\partial S}{\partial R_\alpha}. \tag{2.34}$$

Division by M_α yields the velocity

$$\dot{R}_\alpha = \frac{1}{M_\alpha}\nabla_{R_\alpha} S. \tag{2.35}$$

From equation (2.27) we can derive a continuity equation for the density A^2 by multiplying with $2A$

$$2A\dot{A} = -\frac{2A}{M}\left(\nabla_R A\right)\left(\nabla_R S\right) - A^2\left(\nabla_R^2 S\right)$$

which is equivalent to

$$\frac{\partial A^2}{\partial t} + \nabla_R \left(A^2 \frac{\nabla_R S}{M} \right) = 0 \tag{2.36}$$

and making use of (2.35) we get

$$\frac{\partial A^2}{\partial t} + \nabla_R \left(A^2 \dot{R} \right) = 0, \tag{2.37}$$

with $A^2\dot{R}$ being the current density.

Equations (2.27) and (2.29) describe the motion of a set of non interacting classical particles in the mean field potential of the fast wave function, where the motion of a single particle is given by the Newtonian equation of motion

$$M\ddot{R}(t) = -\nabla_R \left(V_R^{MF}(R) + V_{RR}(R) \right). \tag{2.38}$$

For a complete description we still have to specify the effect of the classical limit upon equation (2.23). We do this by replacing $\psi^\star(R,t)\psi(R,t)$ with a delta function at the slow particle position at time t. Carrying out the integration over R is then leading to

$$i\hbar \frac{\partial \phi(r,t)}{\partial t} = \left[T_r + V_{rr}(r) + V_{rR}(r, R(t)) \right] \phi(r,t) = H_r(r, R(t)) \phi(r,t). \tag{2.39}$$

This is now an explicit time dependent Schrödinger equation due to the time dependence of the slow particle position. The equation (2.38) together with (2.39) define what is sometimes refered as the Ehrenfest method.

For later comparison we now expand the electronic wave function $\phi(r,t)$ in a set of orthonormal basis functions $\phi_i(r,R)$ with parametric dependence on R

$$\phi(r,t) = \sum_i c_i(t) \phi_i(r,R). \tag{2.40}$$

Inserting this into equation (2.39), multiplication from the left with $\phi_j^\star$ and integration over R is leading to

$$i\hbar \dot{c}_j = -i\hbar \sum_i c_i(t) d_{ji}(R) \dot{R}(t) + \sum_i c_i(t) V_{ji}(R), \tag{2.41}$$

where we used the following definitions for the nonadiabatic coupling vector

$$d_{ji}(R) = \int dr \; \phi_j^\star(r,R) \nabla_R \phi_i(r,R) \tag{2.42}$$

and

$$V_{ji}(R) = \int dr \; \phi_j^\star(r,R) H_r(r,R) \phi_i(r,R) \tag{2.43}$$

for the matrix elements of the electronic Hamiltonian. The occupation probabilities of the electronic states are the diagonal elements of the density matrix $a_{ji} \equiv c_j^\star c_i$ and their time evolution is given by

$$\dot{a}_{jj} = \frac{2}{\hbar} \Im \left[c_j^\star c_i V_{ji} \right] - 2\Re \left[c_j^\star c_i d_{ji} \dot{R} \right]. \tag{2.44}$$

If the ϕ_j form an adiabatic basis the off-diagonal matrix elements V_{ji} vanish. We will call the basis set a diabatic basis if the nonadiabatic coupling vector d_{ji} is zero for all values of R, i.e. if the basis functions $\phi_i(r, R)$ are independent of R. For example plane waves form a position independent and thus diabatic basis.

An important aspect of mixed quantum classical methods is whether the energy transfer between the quantum and the classical part is described correctly and if conservation of energy is preserved. The total energy is given by

$$E = \frac{1}{2}M\dot{R}^2(t) + \int dr\ \phi^\star(r,t)H_r(r,R(t))\phi(r,t) \tag{2.45}$$

and taking the time derivative leads to

$$\dot{E} = M\dot{R}\ddot{R} + \left\langle \dot{\phi}\middle| H_r(r,R(t))\middle|\phi\right\rangle + \left\langle \phi\middle| \dot{H}_r(r,R(t))\middle|\phi\right\rangle + \left\langle \phi\middle| H_r(r,R(t))\middle|\dot{\phi}\right\rangle \tag{2.46}$$

where we used the bra-ket notation implying an integration over r and dots are standing for time derivatives. Using equations (2.38), (2.39) and the hermitian conjugate of (2.39) we see that the second and the fourth term on the right side of (2.46) cancel each other and we are left with

$$\dot{E} = -\dot{R}\nabla_R \langle\phi|H_r(r,R(t))|\phi\rangle + \langle\phi|\nabla_R H_r(r,R(t))|\phi\rangle\, \dot{R}, \tag{2.47}$$

where we applied the chain rule in order to get the second term on the righthand side. Now if ϕ is a solution of (2.39) we can apply the Hellmann-Feynman theorem [40]

$$\nabla_R \langle\phi|H_r(r,R(t))|\phi\rangle = \langle\phi|\nabla_R H_r(r,R(t))|\phi\rangle \tag{2.48}$$

and arrive at

$$\dot{E} = 0, \tag{2.49}$$

thus the energy is conserved for the Ehrenfest method.

One drawback of the mixed quantum classical mean field is that it is not possible for a trajectory to split up into trajectories leading to different outcomes. If we imagine a system with two states of which one is the majority channel acquiring most of the occupation probability and the other is the minority state. And if further the outcome for a trajectory propagating on each of this states is completely different, e.g. as illustrated in figure 2.4 sticking and back scattering. Then the movement in the mean field will be dominated by the majority channel and the motion will be close to the corresponding trajectory. Thus leading only to the result of the majority channel (repulsion in our example) and never to the result associated with the minority state.

2.3 Surface Hopping

In contrast to the mean–field method in surface hopping at any time the motion of the classical trajectory is governed by a single electronic state. Surface hopping was first introduced by Preston and Tully [41] as mixed quantum classical method that allows

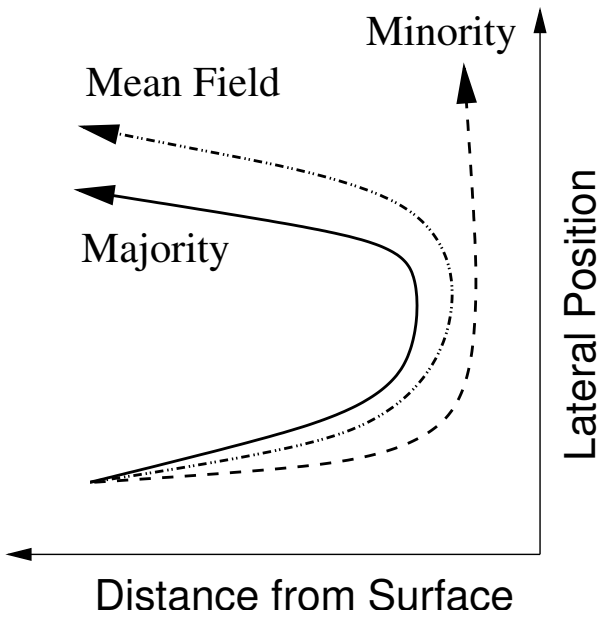

Figure 2.4: The trajectories of an classical particle in the potential of the majority state (solid line), of the minority channel (dashed line) and in the mean field (dot dashed line).

the splitting of trajectories. In this section we will derive surface hopping from the Schrödinger equation (2.8).

As mentioned earlier in surface hopping the wave function is expanded in an orthonormal basis of electronic wave functions $\phi_i(r, R)$, where R is a parameter.

$$\Psi(r, R, t) = \sum_i \psi_i(R, t)\phi_i(r, R). \tag{2.50}$$

Insertion into the Schrödinger-equation (2.8), multiplication with $\phi_j^\star$ from the left and integration over r is leading to a set of coupled equations for the ψ_i's:

$$i\hbar\dot{\psi}_j(R, t) = (T_R + V_{RR})\,\psi_j(R, t)$$

$$+\sum_i \left[V_{ji} - \sum_{\alpha=1}^{3N} \frac{\hbar^2}{2M_\alpha} D_{ji}^\alpha + \sum_{\alpha=1}^{3N} \frac{i\hbar}{M_\alpha} d_{ji}^\alpha \,(i\hbar\nabla_{R_\alpha})\right] \psi_i(R, t). \tag{2.51}$$

Here we introduce the nonadiabatic coupling vectors $D_{ji}^\alpha(R)$ and $d_{ji}^\alpha(R)$ as

$$D_{ji}^\alpha(R) = \left\langle \phi_j(r, R) \middle| \nabla_{R_\alpha}^2 \middle| \phi_i(r, R) \right\rangle \tag{2.52}$$

and analogue to (2.42)

$$d_{ji}^\alpha(R) = \langle \phi_j(r, R) | \nabla_{R_\alpha} | \phi_i(r, R) \rangle \,, \tag{2.53}$$

now making use of the bra-ket notation with integration over the fast coordinates r only. In analogy to (2.43) the matrix elements $V_{ji}(R)$ of the electronic Hamiltonian H_r are given by

$$V_{ji}(R) = \langle \phi_j(r, R) | H_r(r, R) | \phi_i(r, R) \rangle \,, \tag{2.54}$$

where H_r was defined before in (2.21). For notational convenience we will later drop the summation over α as an index of the coordinates as we did with the kinetic energy operator. Now we take the classical limit for the nuclear part of the wave function by splitting $\psi_i(R,t)$ into an amplitude $A_i(R,t)$ and a phase $S_i(R,t)$:

$$\psi_i(R,t) = A_i(R,t)e^{\frac{i}{\hbar}S_i(R,t)}. \tag{2.55}$$

Insertion into equation (2.51) and multiplication with $e^{-\frac{i}{\hbar}S_i(R,t)}$ is leading to

$$i\hbar\dot{A}_j - A_j\dot{S}_j = \tag{2.56}$$

$$-\frac{\hbar^2}{2M}\nabla_R^2 A_j - \frac{i\hbar}{M}\left(\nabla_R A_j\right)\left(\nabla_R S_j\right) + \frac{A_j}{2M}\left(\nabla_R S_j\right)^2 - \frac{i\hbar}{2M}A_j\left(\nabla_R^2 S_j\right) + V_{RR}A_j$$
$$+\sum_i\left[V_{ji}A_i - \frac{\hbar^2}{2M}D_{ji}A_i - \frac{\hbar^2}{M}d_{ji}\left(\nabla_R A_i\right) - \frac{i\hbar}{M}d_{ji}A_i\left(\nabla_R S_i\right)\right]e^{\frac{i}{\hbar}(S_i-S_j)},$$

where again we wrote $\frac{1}{M}\nabla_R$ as an abbreviation of $\sum_{\alpha=1}^{3N}\frac{1}{M_\alpha}\nabla_{R_\alpha}$. This can be split into a pair of equations

$$\dot{S}_j + \frac{1}{2M}\left(\nabla_R S_j\right)^2 + V_{jj} + V_{RR} = \tag{2.57}$$
$$\frac{\hbar^2}{2M}\frac{\nabla_R^2 A_i}{A_j} + \frac{\hbar^2}{2M}\sum_i D_{ji}\frac{A_i}{A_j}e^{\frac{i}{\hbar}(S_i-S_j)} + \frac{\hbar^2}{M}\sum_i d_{ji}\frac{\nabla_R A_i}{A_j}e^{\frac{i}{\hbar}(S_i-S_j)}$$

and

$$\dot{A}_j + \frac{1}{M}\left(\nabla_R A_j\right)\left(\nabla_R S_j\right) + \frac{1}{2M}A_j\left(\nabla_R^2 S_j\right) + \frac{i}{\hbar}\sum_{i\neq j}V_{ji}A_i e^{\frac{i}{\hbar}(S_i-S_j)} \tag{2.58}$$

$$+\frac{1}{M}\sum_i d_{ji}A_i\left(\nabla_R S_i\right)e^{\frac{i}{\hbar}(S_i-S_j)} = 0,$$

where the diagonal elements of $V_{ji}A_i e^{\frac{i}{\hbar}(S_i-S_j)}$ from (2.56) are kept in equation (2.57) and the off-diagonal elements are put into equation (2.58). That choice is somewhat arbitrary, unless we restrict ourself to an adiabatic basis, but still equations (2.57) and (2.58) are equivalent to the original equation (2.56). They also show that $A_j(R,t)$ and $S_j(R,t)$ can no longer be restricted to be real valued functions, due to the contributions from the coupling vectors and the non vanishing phase factors. We now can proceed by taking the classical limit $\hbar \to 0$ of equation (2.57), i.e. the righthand side is set to zero. This is leading to a separate equation for each index j

$$\dot{S}_j + \frac{1}{2M}\left(\nabla_R S_j\right)^2 + V_{jj}(R) + V_{RR}(R) = 0. \tag{2.59}$$

As before in the mean field case this is the Hamilton-Jacobi equation

$$H_j\left(R, \frac{\partial S_j}{\partial R}\right) + \frac{\partial S_j}{\partial t} = 0 \tag{2.60}$$

with an Hamilton function for each state ϕ_j

$$H_j(R,P) = \frac{1}{2M}P^2 + V_{jj}(R) + V_{RR}(R). \tag{2.61}$$

The equations of motion governing the classical particles are then given by

$$M_\alpha \ddot{R}_\alpha(t) = -\nabla_{R_\alpha}\left[V_{jj}(R) + V_{RR}(R)\right]. \tag{2.62}$$

The motion of a nuclear trajectory $R(t)$ is at any time t given by the forces between the classical particles $-\nabla_R V_{RR}$ and the potential V_{jj} of a single state ϕ_j. In which state potential the nuclei are actually moving is determined by the last two terms of equation (2.58) and accomplished by switching between the different state potentials accordingly.

There are some liberties in how to implement the hopping between the potential energy surfaces resulting in various surface hopping versions. For example, in their original paper [41] Tully and Preston allowed jumps only at distinct points in configuration space, namely at the crossings of the diabatic potentials. This has the advantage of eliminating the need to adjust the kinetic energy during a hop, but determining the crossing lines of higher dimensional energy surfaces can be a difficult problem to solve. In contrast to that, the fewest switches algorithm, introduced by Tully in [19], allows switches at any position but requires some form of energy adjustment to recover energy conservation.

In this work we will focus on the fewest switching algorithm, which we will later extend to the method actually used for our simulations. In order to determine the switching probabilities we take a look at $\frac{\partial}{\partial t}A_j^\star A_j$. Using (2.58) we get

$$\frac{\partial}{\partial t}A_j^\star A_j + \nabla_R\left[A_j^\star A_j \Re\left(\frac{\nabla_R S_j}{M}\right)\right] = \tag{2.63}$$

$$\frac{2}{\hbar}\Im\sum_{i\neq j} V_{ji}A_j^\star A_i e^{\frac{i}{\hbar}(S_i - S_j)} - 2\Re\sum_i d_{ji}A_j^\star A_i \frac{\nabla_R S_i}{M} e^{\frac{i}{\hbar}(S_i-S_j)}.$$

If we now compare this with (2.36) and (2.44) we see that the second term is the same as in the continuity equation. Note, that in the classical limit S_j is real valued. This is connected to the interaction between different trajectories evolving in the same electronic state. The third and fourth term appear in (2.44) if we identify c_j with $A_j e^{\frac{i}{\hbar}S_j}$. Thus, if we assume independent trajectories the evolution of the coefficients c_i is given by (2.41).

To summarise the main equations of surface hopping, the nuclear coordinates are given by a time dependent trajectory $R(t)$ and the electronic wave function $\phi(r,t)$ is expanded in a set of orthonormal basis functions $\phi_i(r,R)$ with a parametric dependence on the nuclear coordinates and coefficients $c_i(t)$

$$\phi(r,t) = \sum_i c_i(t)\phi_i\left(r, R(t)\right). \tag{2.64}$$

The time evolution of the coefficients is given by

$$\dot{c}_i(t) = -\sum_j \left\{ c_j(t) \sum_\alpha \left[\dot{R}_\alpha(t) d_{ij}^\alpha \left(R(t)\right) \right] \right\} - \frac{i}{\hbar} \sum_j V_{ij}\left(R(t)\right) c_j(t). \tag{2.65}$$

We now can define the components of the density matrix $a_{ij} \equiv c_i^\star c_j$ with the diagonal elements being the occupation probabilities of the corresponding states. The time derivatives of the a_{ii}'s are given by

$$\dot{a}_{ii} = \sum_j b_{ij} \tag{2.66}$$

where the b_{ij}'s are defined as

$$b_{ij} = \frac{2}{\hbar} \Im \left[a_{ij} V_{ij} \right] - 2\Re \left[a_{ij} d_{ij} \dot{R} \right]. \tag{2.67}$$

Note that the b_{ij}'s are anti symmetric under index interchange $b_{ij} = -b_{ji}$ following from the fact that the d_{ij}'s are anti symmetric as well.

At any given time the system is considered to be in a single basis state, the currently occupied state, which we will denote with ϕ_{occ}. The motion of the slow degrees of freedom is governed by that state

$$\ddot{R}_\alpha(t) = \frac{-1}{M_\alpha} \nabla_{R_\alpha} \left\{ V_{RR}\left(R(t)\right) + \int dr\ \phi_{occ}^\star \left(r, R(t)\right) H_r \left(r, R(t)\right) \phi_{occ}\left(r, R(t)\right) \right\}. \tag{2.68}$$

How the occupied state is determined in the fewest switches algorithm will be discussed in the next section. As already mentioned above this is the point where most surface hopping methods differ. Note also that this set of equations was derived, in a slightly different manner, by Tully in [19] with the assumption that the slow particle movement is given by a trajectory and that the electronic wave function is expanded in the way of (2.64).

One problem with the mixed quantum classical surface hopping is the dependence on the choice of basis functions. Usually we will use the adiabatic basis, but depending on the particular system it is not always clear what would be an optimal basis [18].

2.3.1 Fewest Switches

In Tully's fewest switches algorithm equations (2.65) and (2.62) are integrated simultaneously and, between integration steps, switches between the electronic states are performed, in order to maintain the correct statistical occupation probabilities. This method minimises the number of switches performed. How this is achieved is explained nicely in [19] and we will follow that presentation. If we consider a swarm of N trajectories with occupation probabilities a_{ii} at time t and a'_{ii} at time $t' = t + \Delta t$ then $N_i = a_{ii} N$ and $N'_i = a'_{ii} N$ are the number of trajectories in state i at times t and $t + \Delta t$. The net change of the number of trajectories in state i is then given by

$$\Delta N_i = N'_i - N_i = \left(a'_{ii} - a_{ii}\right) N. \tag{2.69}$$

For short time steps Δt we can replace the difference $a'_{ii} - a_{ii}$ with $\dot{a}_{ii}\Delta t$ and using (2.66) we get

$$\Delta N_i = \dot{a}_{ii}\Delta t N = N\Delta t \sum_j b_{ij}, \tag{2.70}$$

with the state to state transition rates b_{ij} giving the change in state i due to state j, as defined in (2.67). Thus only if b_{ij} is less than zero trajectories jump from state i into state j and their number is given by $N\Delta t b_{ji}$. If we now divide that by the the number of trajectories in state i we get the probability p_{ij} for a trajectory to jump from state i into state j

$$p_{ij} = \frac{N\Delta t b_{ji}}{a_{ii}N} = \Delta t \frac{b_{ji}}{a_{ii}}. \tag{2.71}$$

Note that the switching probabilities are proportional to the time step, thus the total switching probability for a trajectory when passing through a certain region is, apart from an discretisation error, independent of the time steps used. Note also that the probabilities given by (2.71) could in principle get arbitrarily large, but usually the time step required for accurate integration of (2.41) is small and switches will be improbable (see also [17]).

The procedure for the simulation of a single surface hopping trajectory with the fewest switching method can be roughly divided into the following five steps.

Step 1 Set initial conditions for the nuclear coordinates R and velocities $\dot{R}$, the coefficients of the electronic states c_i and choose the currently occupied state.

Step 2 Integrate (2.65) and (2.62) for the time step Δt with the currently occupied state j.

Step 3 According to (2.71) determine the switching probabilities from the current state to all other states. Calculate the p_{ji}'s and set all with $p_{ji} < 0$ to zero (fewest switches). Draw a uniformly distributed random number z in the range of $0 < z < 1$. Jump into the state i for which $\sum_{l=1}^{i-1} p_{jl} < z \leq \sum_{l=1}^{j} p_{jl}$.

Step 4 If a switch to the state l occurs; usually the potential energies $V_{jj}(R)$ and $V_{ll}(R)$ differ at the current position R. To recover energy conservation the velocity is adjusted accordingly in the direction of the nonadiabatic coupling vector $d_{jl}(R)$, for justification of this particular choice see references [42–44]. If the kinetic energy is not sufficient to cover the potential energy difference the the hop is refused and propagation continues on the original potential energy surface.

Step 5 Repeat steps two to four until the trajectory satisfies an appropriate stopping condition.

2.3.2 Energy Conservation and Consistency

In this section we will mention just briefly some problems with the surface hopping approach. While the trajectory stays in one state the total energy of the system is clearly conserved. But one problem is how to retain energy conservation upon a jump

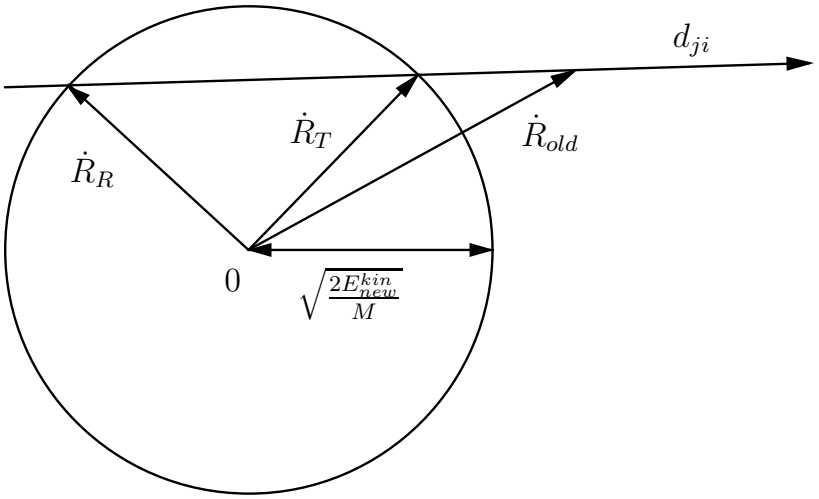

Figure 2.5: Schematic drawing of the rescaling of the velocity in two dimensions after an switch occurred. $\dot{R}_{old}$ is the velocity before the hop and $\dot{R}_T$ and $\dot{R}_R$ are the two new velocities corresponding to the two solutions for λ of (2.72). The radius of the circle is given by the velocity after the jump, where E^{kin}_{new} is the new kinetic energy.

between surfaces with different potential energies. As mentioned above there are some arguments, derived from semiclassical considerations by Pechukas in [45, 46], to adjust the velocity along the nonadiabatic coupling vector in order to compensate for the difference in potential energy. This requires the solution of the following equation

$$0 = \Delta V + \lambda \sum_{\alpha} \frac{\dot{R}_\alpha d^\alpha_{ij}}{M_\alpha} + \lambda^2 \sum_{\alpha} \frac{{d^\alpha_{ij}}^2}{M_\alpha}, \tag{2.72}$$

where ΔV is the change in potential energy and the new velocity is given by $\dot{R}_{new} = \dot{R}_{old} + \lambda d_{ij}$. For a graphical representation see figure 2.5. Usually this equation has two solutions λ and it is not clear which should be used. The solution with the smaller absolute value corresponds to a transmission of the surface normal to d_{ij} and the solution with the larger value is a reflection. As is suggested in [44, 47] we used the λ with the smaller absolute value.

Another problem is that quantum mechanics allows the intrusion of the wave function into classical forbidden areas. This results in hops where there is no solution for (2.72). In the case of such an event one has to either sacrifice consistency, suggesting a hop, or energy conservation. In the fewest switches algorithm energy forbidden hops are rejected thus partially giving up consistency. There is an extensive discussion in the literature about this problem, but to our knowledge no satisfactory solution has been found yet [48, 49].

2.3.3 Generalised Surface Hopping

In 1998, together with Sholl, Tully proposed another method which he called generalised surface hopping. It is a combination of the surface hopping and the mean field

methods [1]. In this method the nuclear degrees of freedom evolve along a classical trajectory $R(t)$ and the electronic wave function is only partially expanded in a finite set of S orthonormal functions ϕ_i and the remainder of the wave function ϕ_C is treated collectively

$$\phi(r,t) = \sum_{i=1}^{S} c_i(t)\phi_i\left(r, R(t)\right) + \phi_C\left(r, R(t)\right). \tag{2.73}$$

The equation of motion for ϕ is given by

$$i\hbar\frac{\partial}{\partial t}\phi(r,t) = H_r\left(r, R(t)\right)\phi(r,t), \tag{2.74}$$

which is a time dependent Schrödinger equation due to the time dependence of $R(t)$. The electronic Hamiltonian H_r was defined before in (2.21). The occupied state ϕ_{occ} can now be either one of the ϕ_i or the collective state ϕ_C. Since the collective state ϕ_C is not necessarily normalised, the equations of motion for the slow particles become

$$\ddot{R}_\alpha(t) = \frac{-1}{M_\alpha}\nabla_{R_\alpha}\left[V_{RR}\left(R(t)\right) + \frac{\int dr\ \phi^\star_{occ}\left(r, R(t)\right) H_r\left(r, R(t)\right)\phi_{occ}\left(r, R(t)\right)}{\int dr\ \phi^\star_{occ}\left(r, R(t)\right)\phi_{occ}\left(r, R(t)\right)}\right]. \tag{2.75}$$

The time evolution of the system is given by equations (2.74) and (2.75) and for the occupation probabilities we get

$$\dot{a}_{ii} = \sum_{j=1}^{S} b_{ij} + b_{iC}, \tag{2.76}$$

with the b_{ij}'s as in (2.67) and b_{iC} defined as

$$b_{iC} = \frac{2}{\hbar}\Im\left[c_i^\star V_{iC}\right] - 2\Re\left[c_i^\star\left\langle\phi_i\middle|\dot{\phi}_C\right\rangle\right]. \tag{2.77}$$

The population $a_{CC} \equiv \langle\phi_C|\phi_C\rangle$ in the collective state is computed using the normalisation of the electronic wavefunction and for the time derivative we get

$$\dot{a}_{CC} = -\sum_{i=1}^{S}\dot{a}_{ii} = -\sum_{i=1}^{S} b_{iC}. \tag{2.78}$$

For the second expression we used (2.76) and the fact that the b_{ij}'s are antisymmetric under index interchange. Note that the generalised surface hopping contains mean field, if $S = 0$, as well as the "classical" surface hopping, if $\phi_C = 0$.

A large drawback of this method is the need for explicit propagation of the wave function according to (2.74). This is usually a much more demanding task than the integration of equation (2.65) since it requires an additional evaluation of the kinetic energy operator.

2.3.4 Surface Hopping with Optical Potential

We now have adopted the generalised surface hopping algorithm in order to address laser-induced reactions at surfaces. Combining ideas of previous treatments [1, 19, 31, 50, 51]. In particular, we have introduced an optical potential in order to simulate the collective influence of electronic excitations of the substrate. The resulting mixed quantum classical method will allow the inclusion of all the relevant nuclear coordinates of both adsorbate and substrate at sufficiently long propagation times to correctly describe thermalization and dissipation effects.

As discussed in the section 2.1 one of the problems encountered when modelling DIET processes with surface hopping algorithms is the huge number of electronic adsorbate and substrate states involved which need to be taken into account. Due to the large number of and similar shapes of the corresponding potentials, it is clear that it is neither feasible to explicitly include all these substrate states into our simulation nor is it necessary since the reaction dynamics is dominated by a few adsorbate states, which must be taken into account. The main effect of the substrate states is coupling different adsorbate states either to each other or to an external electromagnetic field. We model this effect collectively by combining ideas from Tully's fewest switching algorithm [19] and generalised surface hopping method [1] with those of Brenig [31] and Saalfrank [50, 51] who introduced optical potentials to the description of DIET processes.

As with all methods before the Hamilton operator H is split into the kinetic energy T_R of the nuclear coordinates R and an electronic part H_r, where the electronic part depends explicitly on the electronic coordinates r and parametrically on the position of the nuclei R

$$H(r,R) = T_R + H_r(r,R). \tag{2.79}$$

Just as in the generalised surface hopping the electronic wave function Ψ is expanded into the explicitly treated excited adsorbate states ϕ_i and a collective state ψ containing the molecular ground state together with the continuum of substrate excitations

$$\Psi(r,R,t) = \sum_i c_i(t)\phi_i(r,R) + \phi_C(r,R,t). \tag{2.80}$$

The influence of this collective state ϕ_C on the rest of the electronic system can be taken into account by an effective non-Hermitian Hamiltonian (see chapter 16 in [52])

$$H_{eff}(r,R) = T_r + V_{eff}(r,R) + i\Delta(r,R), \tag{2.81}$$

where T_r is the kinetic energy operator of the electrons. The effective potential V_{eff} and the optical potential Δ are real functions of r and R. In a Newns-Andersson picture Δ is related to the lifetime broadening of a resonance state which can be determined via [53]

$$\Delta(E) \;=\; \pi \sum_{\mathbf{k}} |V_{\mathbf{k}}|^2 \delta(E - \varepsilon_{\mathbf{k}}). \tag{2.82}$$

With the effective Hamiltonian and a diabatic (i.e. $\nabla_R \phi_i = 0$) representation of the

wave functions ϕ_i the electronic Schrödinger equation has the following form

$$\dot{c}_j = -\frac{i}{\hbar}\sum_i c_i V_{ji} + \frac{1}{\hbar}\sum_i c_i \Delta_{ji}, \tag{2.83}$$

where the matrix elements V_{ij} and Δ_{ji} are defined as

$$\begin{aligned} V_{ji} &\equiv \langle\phi_j|T_e + V_{eff}(r,R)|\phi_i\rangle \\ \Delta_{ji} &\equiv \langle\phi_j|\Delta(r,R)|\phi_i\rangle \ , \end{aligned} \tag{2.84}$$

respectively. For the diagonal elements of the density matrix a_{ji} this leads to

$$\dot{a}_{jj} = \sum_i b_{ji} + \sum_i \frac{2}{\hbar}\Re\left[a_{ji}\Delta_{ji}\right], \tag{2.85}$$

with $b_{ji} \equiv \frac{2}{\hbar}\Im\left[a_{ji}V_{ji}\right]$ and the density matrix elements defined as before. Note that for a normalised wave function Ψ the occupation probability a_{cc} for the "rest" is simply given by $a_{cc} \equiv 1 - \sum_j a_{jj}$, leading to

$$\dot{a}_{cc} = -\sum_j \dot{a}_{jj} = -\frac{2}{\hbar}\sum_{ij}\Re\left[a_{ji}\Delta_{ji}\right], \tag{2.86}$$

since $\sum_{ji} b_{ji} = 0$. The classically treated nuclear coordinates R obey formally the same Newtonian equation of motion as for the generalised surface hopping

$$\ddot{R} = \frac{-1}{M}\nabla\left[\frac{\langle\phi_{occ}|H_e|\phi_{occ}\rangle}{\langle\phi_{occ}|\phi_{occ}\rangle}\right], \tag{2.87}$$

where ϕ_{occ} is the currently occupied state. In order to determine both the classical and the quantum dynamics are determined self-consistently, the equations (2.83) and (2.87) need to be integrated simultaneously while the currently occupied state is determined via the fewest switching algorithm. The probabilities for hops between the different potentials $\langle\psi_{occ}|H_e|\psi_{occ}\rangle\,/\,\langle\psi_{occ}|\psi_{occ}\rangle$ for the classical motion are, for jumps between explicitly treated states

$$p_{ji} = \frac{\Delta t\, 2Im(a_{ij}V_{ij})}{\hbar a_{jj}}, \tag{2.88}$$

and the probability to go from state j to the collective state ϕ_C is given by

$$p_{jC} = \frac{-2\Delta t}{\hbar a_{jj}}\sum_i a_{ji}\Delta_{ji}. \tag{2.89}$$

As in the fewest switches surface hopping switches between the states can occur at any point along the classical trajectories $R(t)$. Note that switches into the collective state occur only if the sum $\sum_i a_{ji}\Delta_{ji}$ is negative. We will also use this formalism to describe the excitation from the collective state into a particular electronic state j. For such a transition the sum in 2.89 has to be positive, i.e. the sign of the optical potential has

to be reversed. In order to simulated the excitation by a short laser pulse the optical potential needs to be time dependent which is a straight forward generalisation.

This approach differs from the generalised surface hooping of the previous section in some points. First, we have introduced an optical potential in order to describe transitions to the collective state ψ. Furthermore we assume that the whole excess energy upon a transition to or from the continuum state is taken up by the substrate electrons, as it is usually done in the modelling of laser-induced desorption [16]. This means that upon a switch to the continuum state we just make a Franck-Condon transition, i.e. we transfer the molecule to the ground state potential with its kinetic energy preserved and perform ordinary Born-Oppenheimer molecular dynamics until the final fate of the molecule has been determined.

If just one electronically excited state is considered, then the equations become much simpler. According to eqs. (2.85) and (2.86), the de-excitation rate is directly given by

$$\dot{a}_{11} \;=\; -\dot{a}_{cc} \;=\; \dot{c}_1 c_1^* + c_1 \dot{c}_1^* = \frac{2a_{11}\Delta(R)}{\hbar}. \tag{2.90}$$

In fact, for such a situation no electronic Schrödinger equation has to be integrated, leading to much shorter computation times.

2.4 Simulation of Quantum Properties with Classical Mechanics

In this section we will highlight two difficulties encountered when trying to simulate quantum mechanical quantities with classical trajectories. One is the choice of initial conditions and the other the assignment of continuous classical results to discrete quantum numbers such as rotational momentum.

2.4.1 Initial Conditions

In order to derive probabilities from classical simulations one has to average over different initial conditions. Now the question arises how to weight each point in phase space. In quantum mechanics there is no simultaneous probability distribution for position and momentum due to the uncertainty principle. Wigner discussed this problem in [54] and showed that the function $P(x,p)$ defined as

$$P(x,p) = \left(\frac{1}{\hbar\pi}\right)^n \int d^n\mathbf{y}\Psi^\star(\mathbf{x}+\mathbf{y})\Psi(\mathbf{x}-\mathbf{y})e^{2i\frac{\mathbf{py}}{\hbar}} \tag{2.91}$$

has all the properties requested of simultaneous probability distribution of the classical positions $\mathbf{x} = (x_1, x_2, \ldots, x_{n-1}, x_n)$ and momenta $\mathbf{p} = (p_1, p_2, \ldots, p_{n-1}, p_n)$, such as giving the correct probabilities for x when integrated over p and vice versa. $\Psi(\mathbf{x})$ is the initial quantum mechanical wave function and the integration is over the whole space.

If for the wave function we insert the ground state solution of an one dimensional harmonic oscillator $\Psi(x) = \frac{1}{\sqrt{x_0\sqrt{\pi}}} e^{-\frac{1}{2}\left(\frac{x}{x_0}\right)^2}$ into equation (2.91) we get

$$P(x,p) = \frac{1}{\sqrt{\pi}x_0} e^{-\frac{x^2}{x_0^2}} \frac{x_0}{\sqrt{\pi}\hbar} e^{-\left(\frac{px_0}{\hbar}\right)^2}, \tag{2.92}$$

which is the product of two independent Gaussian distributions with width $\sigma_x = \frac{x_0}{\sqrt{2}}$ for the position x and width $\sigma_p = \frac{\hbar}{\sqrt{2}x_0}$ for the momentum. Here the characteristic length x_0 is given by $x_0 = \sqrt{\frac{\hbar}{\omega m}}$ with ω being the frequency and m the mass of the oscillator [55]. If we use the relation $\frac{\partial^2 V}{\partial^2 x} = m\omega^2$ between the second derivative of the potential V, the mass m and the frequency ω we get for x_0

$$x_0 = \frac{\sqrt{\hbar}}{\sqrt[4]{m\partial_x^2 V}}, \tag{2.93}$$

and consequently

$$\sigma_x = \sqrt{\frac{\hbar}{2\sqrt{m\partial_x^2 V}}} \tag{2.94}$$

and

$$\sigma_p = \sqrt{\frac{\hbar\sqrt{m\partial_x^2 V}}{2}}. \tag{2.95}$$

Due to the large masses of the molecules involved in our simulations, the width of the position distribution usually is small and the potential can be approximated to be harmonic at the minimum. Therefore we always use normal distributed initial positions and momenta according to equations (2.92), (2.94) and (2.95). For systems with more than one degree of freedom we first calculate the normal modes by diagonalising the Hessian matrix of the ground state potential and then determine the initial conditions for the normal modes with widths according to the corresponding frequencies.

2.4.2 Mapping Classical Quantities to Quantum Numbers

Another problem encountered when comparing the results of classical simulations with quantum mechanical calculations or state resolved measurements is that of mapping the continuous classical quantities onto discrete quantum numbers. We always associated the classical quantity with the nearest corresponding quantum number. In particular for rotation the rotational energy E_{rot} of a diatomic molecule as a function of the rotational quantum number j is given by

$$E_{rot}(j) = \frac{\hbar^2}{2mr_0^2} j(j+1), \tag{2.96}$$

where the effects of intra molecular vibration are neglected. m is the reduced mass and r_0 the equilibrium atom-atom distance of the molecule and $j \in \mathbb{N}_0$. Consequently trajectories with rotational energies in the range corresponding to the interval $\left[j - \frac{1}{2}, j + \frac{1}{2}\right[$ are assigned to j. Note, for NO in it's ground state we have $\frac{\hbar^2}{2mr_0^2} \approx 0.21$ meV.

For vibrational coordinates we distinguish between harmonic potentials and those in a Morse potential. In the harmonic case the energy $E_{harm.}$ of a quantum mechanical oscillator with quantum number n is given by $E_{harm.} = \hbar\omega\left(n + \frac{1}{2}\right)$ and thus trajectories with energies, kinetic and potential, in the range of the interval $[\hbar\omega n, \hbar\omega(n+1)[$ are mapped to n where ω is the oscillator frequency connected to the second derivative V'' of the potential at the minimum via $\omega = \sqrt{\frac{V''}{m}}$ and m is the corresponding mass. In the case of vibration of a particle with mass m in a Morse potential given by

$$V(x) = V_0\left(1 - e^{-\alpha(x-x_0)}\right)^2 \tag{2.97}$$

the quantum mechanical energies need to be corrected due to anharmonicity of the potential and are [56]

$$E_{Morse}(n) = \hbar\sqrt{\frac{2\alpha^2 V_0}{m}}\left(n + \frac{1}{2}\right) - \frac{\hbar^2\alpha^2}{2m}\left(n + \frac{1}{2}\right)^2, \tag{2.98}$$

and we map the interval $\left[E_{Morse}(n - \frac{1}{2}), E_{Morse}(n + \frac{1}{2})\right[$ to n. The corresponding frequency is given by $\omega_{Morse} = \sqrt{\frac{2\alpha^2 V_0}{m}}$. The correction due to the anharmonicity is small, especially for small n, and only plays a role for highly excited states.

Chapter 3

A Simple Model System

In this chapter we will investigate a simple one dimensional model system in order to gain some insight about the fundamental mechanisms in laser induced desorption. Due to the restricted dimensionality a simple model certainly can not be expected to reproduce momentum distributions, since no energy transfer between different degrees of freedom is possible. But it might help to understand the dependence of the desorption probability on the most characteristic numbers of the bond between adsorbate molecule and surface, namely binding energy in both the ground and the excited state, the relative position of the minima and the lifetime in the excited state.

Laser induced desorption experiments of NO from small Pd-clusters supported by an alumina substrate were performed by Kampling et al. [20]. They observed a strong (one order of magnitude) variation of the desorption yield with cluster size. Temperature programmed desorption spectra indicate slightly different adsorption energies of the NO for different cluster sizes (see figure 3.1). The observed desorption maxima correspond to binding energies between 0.70eV and 0.75eV. In order to investigate whether these differences in the binding energy could account for a sufficiently large change in desorption probability we performed some simple simulations.

3.1 Model and Simulation

To simulate the desorption process of NO from the small Pd-clusters we used the simplest possible model, a one dimensional two state model with a fixed excited state lifetime, Frank-Condon transitions and a single excitation. For the representation of the potentials we used Morse-potentials of the following from

$$V_{Morse}(x) = a\left(e^{-2cx} - 2e^{-cx}\right). \tag{3.1}$$

Note that we choose the inverse decay length c as a parameter instead of setting the decay length $1/c$, this allows for constant potentials by setting c equal to zero, causing

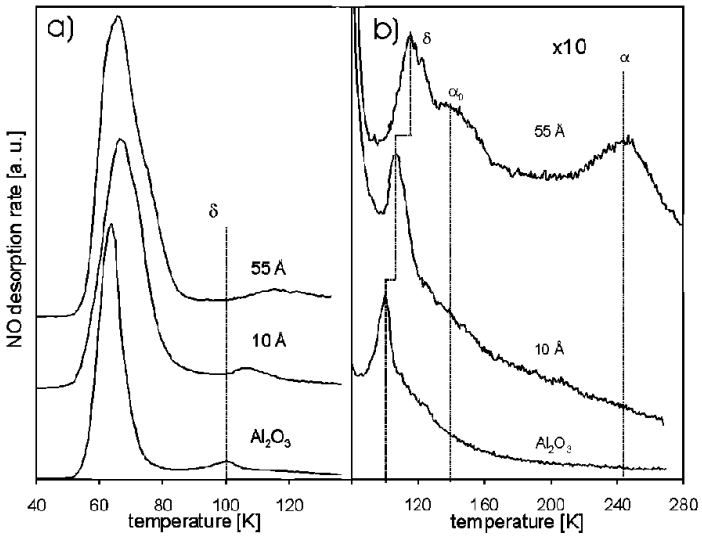

Figure 3.1: Temperature programmed desorption spectra of NO from different sized Pd-clusters and the Al_2O_3 substrate, from [20].

less numerical problems than setting $1/c$ to infinity. Thus we have five parameters characterising the potentials, the strength a and the range parameter c for the ground and the excited state and the distance between the minima Δx, where the excited state potential is given by $V^e(x) = V_{Morse}\,(x - \Delta x)$. Thus values of $\Delta x > 0$ correspond to an MGR-like situation while a $\Delta x < 0$ is leading to an Antoniewicz scenario. Another important parameter is the lifetime in the excited state τ. With that the probability $P_{ex}(t)$ of the adsorbate still being in the excited state at time t after excitation at time zero is given by

$$P_{ex}(t) = \frac{1}{\tau} e^{-\frac{t}{\tau}}. \tag{3.2}$$

This is equivalent to the assumption of a constant optical potential with strength $\Delta(x) = \frac{\hbar}{2\tau}$. The last parameter is the mass of the adsorbate molecule, but this is connected to the length scale used.

A important feature of the Morse potential is the fact, that the classical equation of motion can be solved analytical, see references [57, 58]. For energies larger than zero we use the following ansatz

$$x(t) = A \ln\left(B \cosh(Ct) - D\right). \tag{3.3}$$

If we insert this into the equation of motion

$$M\ddot{x}(t) = -\frac{d}{dx} V_{Morse}\left(x(t)\right) \tag{3.4}$$

we get a set of equations for A, B, C and D which are solved by

$$A = \frac{1}{c}, \tag{3.5}$$

$$B = \left(\frac{E}{a} \sqrt{\frac{a}{E+a}} \right)^{-1}, \tag{3.6}$$

$$C = c\sqrt{\frac{2E}{m}}, \tag{3.7}$$

and

$$D = \frac{a}{E}. \tag{3.8}$$

For bound solutions, i.e. energy $E < 0$, the solution is of the form

$$x(t) = A \ln \left(B \cos(Ct) - D \right), \tag{3.9}$$

where the hyperbolic cosine is replaced by an cosine reflecting the periodic nature of the bound solutions. The parameters A, B and D are the same as for the free solution. Only in C we have to change the sign of the energy

$$C = c\sqrt{\frac{-2E}{m}}. \tag{3.10}$$

These solutions are for the initial conditions of $x(t=0) = x_{TP}$ and $\dot{x}(t=0) = 0$, where x_{TP} is the inner turning point which is given by the negative solution of equation

$$V_{Morse}\left(x_{TP}\right) \equiv E. \tag{3.11}$$

This equation has no solution for $E < -a$ and two solutions for $a \leq E \leq 0$

$$x_{TP} = -\frac{1}{c} \ln \left(1 \pm \sqrt{1 + \frac{E}{a}} \right). \tag{3.12}$$

For $E > 0$ only the solution with the plus sign is a valid one. The inner solution, for energies larger $-a$, is always the one with the plus sign. The solutions for arbitrary initial conditions can be found by first calculating the corresponding energy. From that and the initial position an corresponding offset time $t_{initial}$ can be calculated by inverting either (3.3) or (3.9). For the correct solutions this time must then be added to the propagation time.

Thus for each initial position x_i and velocity v_i we can calculate the position $x_f(x_i, v_i, t_{res})$ and velocity $v_f(x_i, v_i, t_{res})$ after propagation in the excited state for the residence time t_{res}. Since we do not include any dissipation mechanism, a trajectory then would desorb if it's final energy

$$E_f = E_f\left(x_i, v_i, t_{res}\right) = V_{Morse}^{ground}(x_f) + \frac{1}{2M} v_f^2 \tag{3.13}$$

is larger than zero. The desorption probability P_{des} can be calculated by integration over all initial positions and velocities and all residence times corresponding to a positive final energy weighted with an appropriate probability density $\rho\left(x_i, v_i, t_{res}\right)$

$$P_{des} = \int dx_i \int dv_i \int_0^\infty dt_{res} \Theta\left(E_f\left(x_i, v_i, t_{res}\right)\right) \rho\left(x_i, v_i, t_{res}\right), \tag{3.14}$$

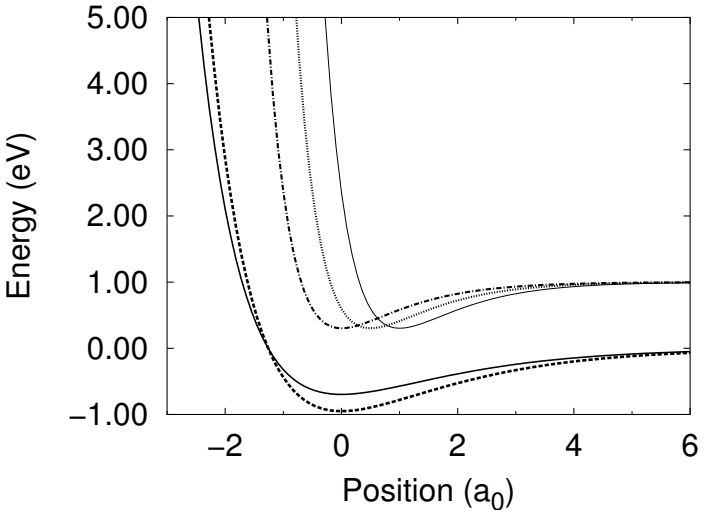

Figure 3.2: Some of the model potentials used in our calculations. The lower two potentials have an inverse decay length c of 0.55 a_0^{-1} with a depth of 0.70 eV (solid line) and 0.95 eV (long dashed line). The upper three are shifted up by 1.0eV for better visibility and have a binding energy of 0.70 eV and a c-parameter of 1.0 a_0^{-1} and are shifted to the right by 0.0 a_0, 0.5 a_0 and 1.0 a_0.

where $\Theta(x)$ is the Heaviside step function. To evaluate (3.14) we sample the integrant at discrete positions, momenta and residence times and replace the integrals by sums over the sampling points. The weights for the position and the velocity are given by Gaussian distributions as discussed in section 2.4.1, whereas the weights for the lifetime can be derived from equation (3.2). We checked the validity of the harmonic approximation for the initial distribution with parameters later used in our simulation by investigating its time evolution. We found the shape of the position and momentum distribution to be stationary indicating that indeed in the range of the initial position distribution the potential at the minimum is nearly harmonic. Note that for an NO molecule with a spatial distribution width of $\sigma_{pos} = 0.1$ a_0 the energy associated with the corresponding momentum distribution is only 6.2 meV.

3.2 Parameter Dependence

In this section we discuss the variation of the desorption probability in our simple model with the different potential parameters. For the mass we always chose the mass of the $^{14}N^{16}O$ molecule. Unless stated otherwise we used an excited state lifetime of $\tau = 12.095$ fs $= 500$ a.u. This seems to be a reasonable value for the lifetime of an excited adsorbate state in front of an insulator where resonant tunnelling should not play a role [6, 59]. On metals excited state lifetimes are usually much shorter in the order of a few femtoseconds [60]. Typical potentials used are depicted in figure 3.2.

The change of the desorption probability with the binding energy of the ground state is shown for two different values of Δx in the left graph of figure 3.3. As one

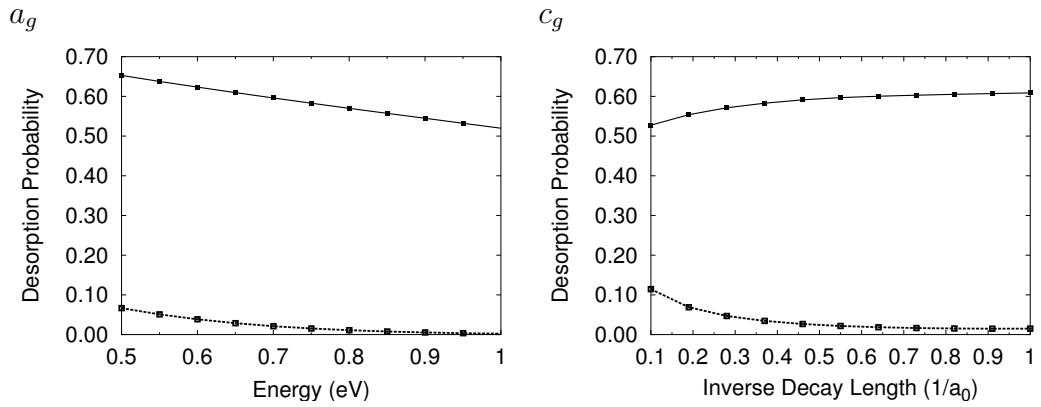

Figure 3.3: These graphs show the change of desorption probability with the ground state parameters for different minimum displacements. The left graph, labelled a_g shows the variation with the ground state binding energy and in the right one, labelled c_g, we can see the dependence on the inverse ground state decay length. For the parameters used see table 3.1.

line type	a_g [eV]	c_g [a_0^{-1}]	a_e [eV]	c_e [a_0^{-1}]	Δx [a_0]
solid	0.70	0.55	0.70	1.0	1.0
dashed	0.70	0.55	0.70	1.0	0.5

Table 3.1: Parameters for figures 3.3 and 3.4

would expect, it decreases with increasing binding energy. However, for reasonable parameters, the change in desorption probability is not large enough to account for the experimentally observed change in desorption yield. The dependence on the width of the ground state potential shown in the right half of figure 3.3 is more interesting. For the curve with the large Δx (solid line) and subsequently larger desorption probability we see an increase followed by a saturation. Whereas in the case with the lower Δx we observe an initial drop and also an levelling off for larger c_g. This behaviour can be understood by looking at the corresponding potential changes and the desorption probability as a function of initial position. Small values of c_g correspond to a rather wide ground state potential and thus a large width σ_{pos} of the initial position distribution. Large c_g's on the other hand characterise a very narrow potential and thus a small initial width. In the current case we have $\sigma_{pos} = 0.307$ a_0 for $c_g = 0.1$ a_0^{-1} and $\sigma_{pos} = 0.097$ a_0 for $c_g = 1.0$ a_0^{-1}. We now can compare this with the desorption probability as a function of initial position (compare figure 3.4). We see that for $\Delta x = 1.0$ a_0 there is a non vanishing desorption probability of approximately 0.60 at $x_i = 0.0$ a_0, while for $\Delta x = 0.5$ a_0 it is zero. Thus with increasing concentration of the initial position distribution around the centre the total desorption probability approaches the desorption probability at $x = 0$. This immediately explains the drop of the desorption probability for the $\Delta x = 0.5$ a_0 case. For the $\Delta x = 1.0$ a_0 case things are more complicated. The gain in probability for positive initial positions is accompanied by a loss for negative x_i. But since the slope of the curve in figure 3.4 is larger for positive

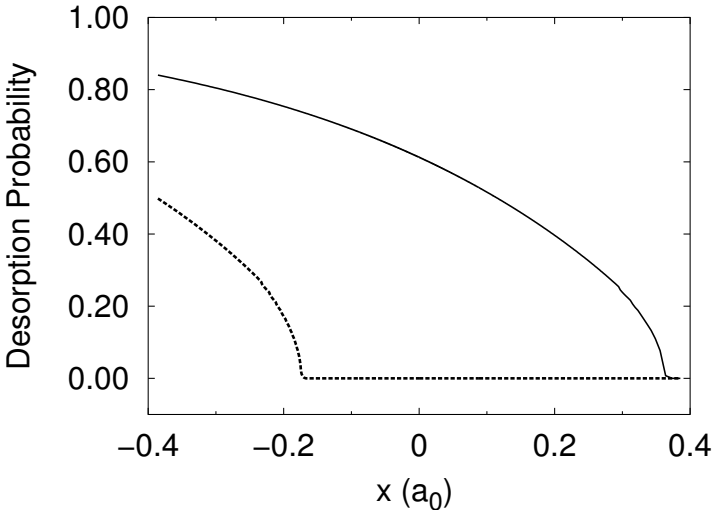

Figure 3.4: This graph shows the dependence of the desorption probability on the initial position. The parameters and the line styles used are given in table 3.1.

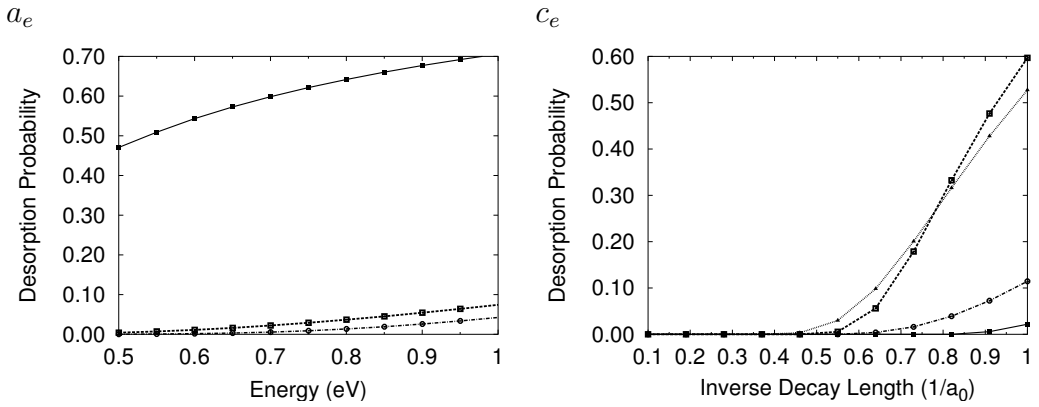

Figure 3.5: Basically the same as fig. 3.3 but for the excited state parameters. For the parameters for the a_e-dependence see table 3.2 and table 3.3 for c_e parameters

values the net effect is a rise in the desorption probability for narrower distributions. The change in desorption probability due to different width of the momentum distribution is negligible since the width is rather small, in the order of a few meV, and over the range of initial velocities, with significant contributions to (3.14), the desorption probability is almost constant.

Next we take a look at the dependence on the excited state parameters. Again the change in desorption probability with increasing binding energy of the excited state behaves as one would expect, compare the left graph in figure 3.5. The forces $F(x) = -\nabla V_{Morse}(x)$ acting on a particle moving in a Morse potential of the form (3.1) are given by

$$F(x) = 2ac\left(e^{-2cx} - e^{-cx}\right) \tag{3.15}$$

and as the binding energy increases the desorption probability is increasing as well since

line type	a_g [eV]	c_g [a_0^{-1}]	c_e [a_0^{-1}]	Δx [a_0]
solid	0.70	0.55	1.00	1.0
dashed	0.70	0.55	1.00	0.5
dot dashed	0.70	0.55	0.55	1.0

Table 3.2: Parameters for the left panel of figure 3.5

line type	a_g [eV]	c_g [a_0^{-1}]	a_e [eV]	Δx [a_0]
solid	0.70	0.55	0.70	0.5
dashed	0.70	0.55	0.70	1.0
dot dashed	0.70	0.10	0.70	0.5
dotted	0.70	0.10	0.70	1.0

Table 3.3: Parameters for the right panel of figure 3.5

the forces accelerating the adsorbate are proportional to the binding energy resulting in an higher energy gain and ultimately more desorption.

For the dependence on the inverse decay length we have a similar picture. The desorption probability goes up with increasing c_e, see the right graph in figure 3.5. This again is due to larger forces with increasing c_e resulting in a larger energy gain and consequently leading to a larger desorption probability. But this time the slope of the curves for the potentials with large Δx are much larger and a small change in the parameter could account for a rather large change in desorption probability.

The last potential parameter to discuss is the separation of the minima. In figure 3.6 we show the desorption probability as a function of Δx for different parameter sets. For the MGR scenarios (positive Δx) the desorption probability is increasing fast with the separation of the minima. This can be understood considering the fact that transitions between the different electronic states are Frank-Condon like and thus for larger positive Δx the trajectories start further up the repulsive wall of the excited state potential, where the resulting forces are large. For wide distributions of the initial positions, i.e. small c_g, the rise is less steep but with an earlier onset as for narrow ground state potentials. For the Antoniewicz schemes the situation is different. The desorption probabilities are much smaller than for the MGR scenarios and only for a rather large binding energy in the excited state we get considerable desorption. This is again related to the forces at the Frank-Condon point. For the small binding energies the potential is very flat to the right side of the minimum. Only for large potential depth the molecules gain enough energy to desorb.

After analysing the dependence of the desorption probability on the potential parameters we still have to look at the excited state lifetime. As we can see in the graphs of figure 3.7, the dependence of the desorption probability on the lifetime is showing a fast initial increase for the MGR scenarios followed by a saturation, while for Antoniewicz like cases we still have a saturation level but that is reached for much larger lifetimes. This behaviour is best analysed by looking at the desorption probability as a function of the residence time in the excited state, as depicted in the

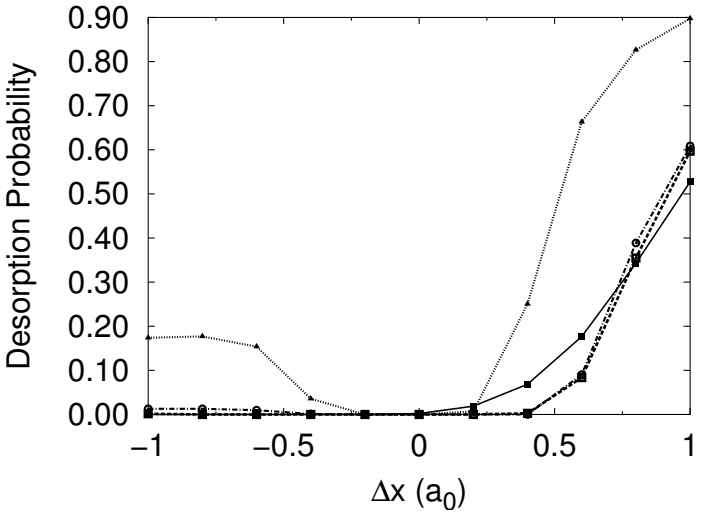

Figure 3.6: The dependence of the desorption probability on the separation of the minima. Parameters used are for the solid line $c_g = 0.1$ a_0^{-1}, for the dashed line $c_g = 0.55$ a_0^{-1}, the dot dashed line corresponds to $c_g = 1.0$ a_0^{-1} and for the dotted line with the triangles we also used $c_g = 1.0$ a_0^{-1} but with a larger binding energy of $a_e = 3.0$ eV. The other parameters we used were $a_g = 0.70$ eV, $a_e = 0.70$ eV, $c_e = 1.0$ a_0^{-1} and $\Delta x = 0.5$ a_0.

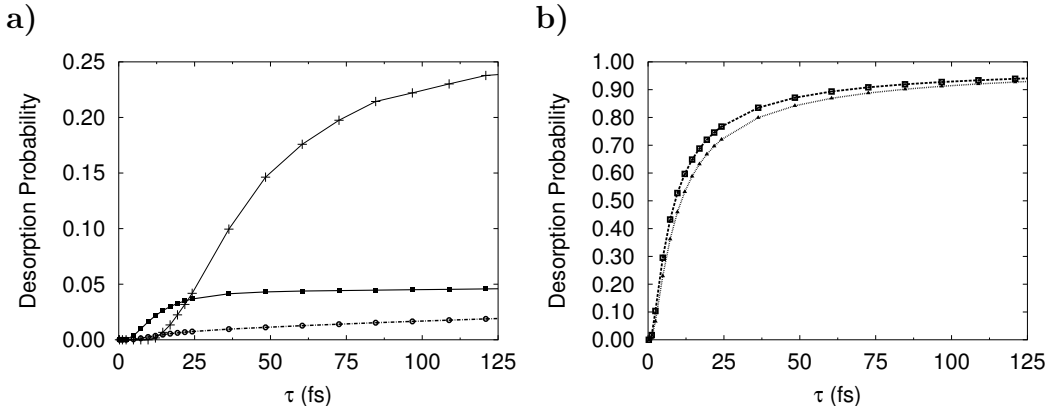

Figure 3.7: Variation of the desorption probability with the excited state lifetime τ. The corresponding parameters are given in table 3.4.

figure 3.8. For all scenarios we have a certain offset residence time below which there is no desorption. Since for all cases some time is required for the adsorbate to be in the excited state before they gained enough energy to overcome the desorption barrier. The Menzel-Gomer-Redhead scenarios then show a fast increase and in some cases some overshooting before reaching a saturation level. This is because most trajectories are at the repulsive part of the excited state after the initial excitation and gain enough kinetic energy to overcome the excited state binding energy and only a few will start to oscillate. In the Antoniewicz case the picture is very different instead of reaching a constant plateau the desorption probability is oscillating, which is connected to the

line type	point type	a_g [eV]	c_g [a_0^{-1}]	a_e [eV]	c_e [a_0^{-1}]	Δx [a_0]
thick solid	squares	0.70	0.55	0.70	1.0	0.5
thin solid	crosses	0.70	0.55	0.70	1.0	-1.0
dot dashed	circles	0.95	0.55	0.70	1.0	0.5
dashed	squares	0.70	0.55	0.70	1.0	1.0
dotted	triangle	0.95	0.55	0.70	1.0	1.0

Table 3.4: Parameters for figures 3.7 and 3.8.

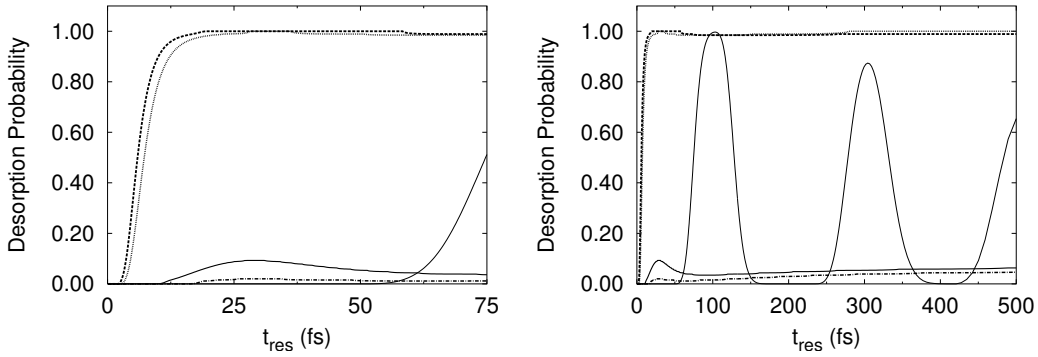

Figure 3.8: The desorption probability for different residence times, i.e. in equation (3.14) we integrated only initial position and momentum. The left graph shows an enlargement. The parameter set used was the same as for the graphs in figure 3.7 and is given in table 3.4.

fact that the Franck-Condon transition into the excited state is to the attractive part of the potential. Thus, in contrast to the MGR scenario the majority of trajectories is trapped in the excited state and starts to oscillate.

3.3 Isotope Effect

The last aspect of the simple one dimensional model we want to explore is the dependence of the desorption probability on the particle mass and the accuracy of the simple model for the isotope effect as given by eq. (2.3). We do this for three potential parameter sets with different minimum separation, which we also used in the previous section. The potentials are shown in figure 3.9 and the corresponding desorption prob-

$\Delta x(a_0)$	-1.0	0.5	1.0
$P_{des}(\%)$	0.166	2.169	59.684

Table 3.5: The desorption probabilities for different minimum separations. The particle mass used was 30 amu and the remaining potential parameters were $a_g = 0.70$ eV, $c_g = 0.55$ a_0^{-1}, $a_e = 0.70$ eV and $c_e = 1.0$ a_0^{-1}

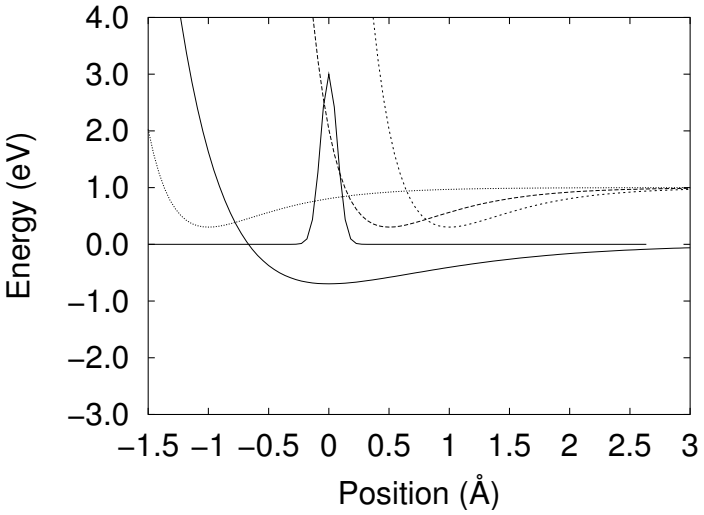

Figure 3.9: The potentials corresponding to figure 3.10 and a typical initial position distribution in the ground state for a particle mass with the mass of an NO molecule. The parameters used are $a_g = 0.70$ eV, $c_g = 0.55$ a_0^{-1}, $a_e = 0.70$ eV, $c_e = 1.0$ a_0^{-1} and -1.0, 0.5 and 1.0 a_0 for Δx. The excited state potentials are shifted up by 1 eV for better clarity.

$\Delta x = 0.5$ $\mathbf{a}_0$ $\Delta x = 1.0$ $\mathbf{a}_0$ $\Delta x = -1.0$ $\mathbf{a}_0$

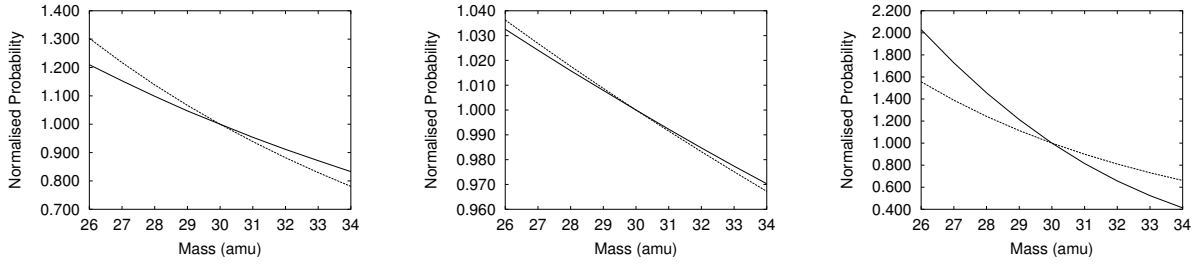

Figure 3.10: The desorption probability as a function of particle mass for three different minimum separations (solid line). The probabilities are normalised to the probability at $m = 30$ amu, the corresponding numbers are given in table 3.5. Also shown, with the dashed line, is the scaling factor according to equations (2.3). The remaining potential parameters are $a_g = 0.70$ eV, $c_g = 0.55$ a_0^{-1}, $a_e = 0.70$ eV and $c_e = 1.0$ a_0^{-1}

abilities for the $^{14}N^{16}O$ mass are given in table 3.5. The dependence of the desorption on the particle mass is depicted in figure 3.10 together with the results from equation (2.3). As can be seen from these graphs, the simple model is most accurate for the largest desorption probability at $\Delta x = 1.0$ a_0 and the least accurate for the smallest desorption yield in the Antoniewicz scenario.

The deviations from equation (2.3) can be understood by analysing the assumptions used in the derivation. Explicitly we assumed a linear excited state potential, for $\Delta x = 1.0$ a_0 this seems to be reasonable. But if we look at the potential curves in figure 3.9 for $\Delta x = 0.5$ a_0 and $\Delta x = -1.0$ a_0 we see that the slope varies over

the width of the distribution of the initial position. In particular for the MGR like scenarios the slope decreases in the direction of the force, while in the Antoniewicz scenario it increases. Thus for lighter molecules in the MGR case the acceleration will decrease faster than for the heavier ones, leading to a reduction of the mass effect, while in the Antoniewicz model most of the light molecules will see larger forces faster, increasing the separation with the heavier ones. This can explain the fact that in the case of the Antoniewicz scenario the simple model underestimates the isotope effect and for the MGR schemes it over estimates it. Another effect we neglected was the fact the with the particle mass the width of the initial distribution changes. This will be particularly important if the desorption probability is small, since in such cases most desorption comes from the tails of the initial distribution where the effect of a different width is largest. Thus lighter particles will see larger desorption probabilities than expected while for the heavier molecules the desorption probability will be smaller than suggested by (2.3).

In this chapter we showed that even a relatively simple one dimensional two-state model for the laser induced desorption can, while using reasonable parameters, produce nearly all possible desorption probabilities between zero and one. We find the most important parameters to be the separation between the minima of the ground and the excited state potential, the length scale of the excited state and the excited state lifetime. Changes in these parameters could account for the variations in desorption probability as observed in the experiment. Thus a realistic simulation of the laser induced desorption probability of NO from small supported Pd clusters would require the ab initio calculation of the binding geometry and energy for the ground state and relevant excited states. Furthermore it would be necessary to investigate the influence of the cluster size on quenching process. Since the lifetime of the excited state is dependent on the electronic structure of the clusters, it might be the reason for the observed desorption yield changes.

Chapter 4

Laser-Induced Desorption of NO from NiO

In this chapter we will use the modified surface hopping with optical potential introduced in chapter 2 to investigate the laser induced desorption of NO from a NiO (100) surface. This system is very interesting for several reasons. First of all the experimentally observed desorption cross section is several orders of magnitude larger than that from metal substrates (10^{-17}cm^2 vs 10^{-21}cm^2 [61]). Second, the momentum distribution of the desorbed NO molecules shows an interesting bimodality, the origin of which should be explained by theory. And, particular in connection with this work, there exist analytical expressions for the potential energy surfaces of the ground state and one charge transfer state as a function of the centre of mass distance from the surface and the polar angle, derived from ab initio calculations by Staemmler et al. [2, 62]. They also performed wave packet simulations of the desorption on these potentials [3], which will serve as as a benchmark for our mixed quantum classical method.

We will first present some of the experimental facts about the laser induced desorption of NO from a NiO(100) surface. Then we will present the potential energy surfaces on which our simulations are based. After that we will discuss wave packet results from [3] and compare the results with our mixed quantum classical calculations. We will conclude with a more detailed discussion of the mixed quantum classical results using extended potentials, friction and alternative excitation schemes.

4.1 Experiments

The laser induced desorption of NO from a NiO(100) surface has been well-studied experimentally [7, 61, 63–66]. The experiments are performed either on thin NiO films grown on the (100) surface of a Ni single crystal or on the surface of a cleaved NiO crystal. A comparison between the desorption of NO from thin oxide films or from NiO crystals showed nearly no differences [63]. From the NiO(100) surface NO molecules

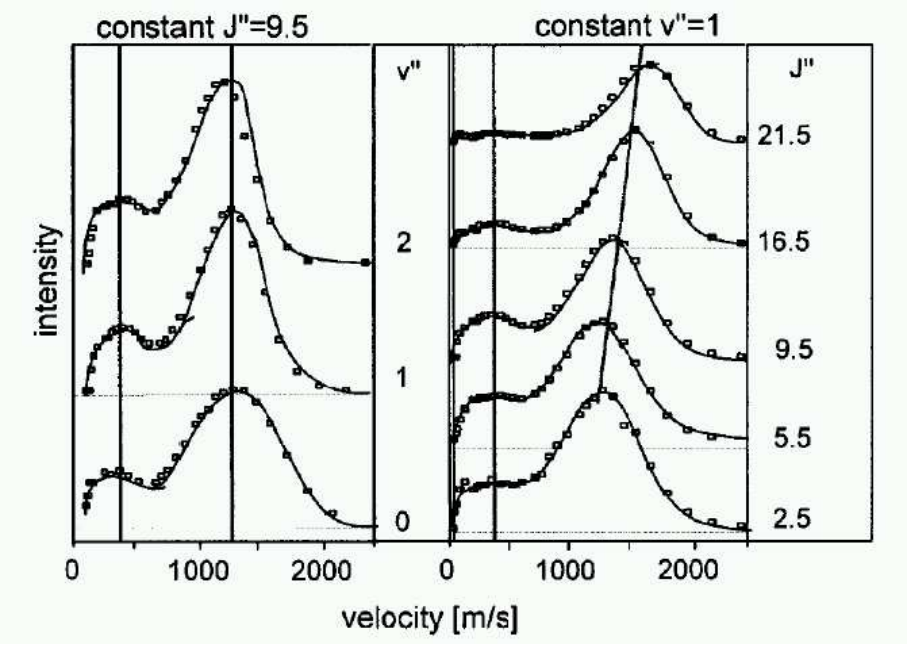

Figure 4.1: The experimental NO momentum distributions for different vibrational and rotational states as measured by [61] (taken from [3])

thermally desorb at at about 220 K [63], corresponding to a binding energy of 0.52 eV. NEXAFS (near edge x-ray adsorption fine structure) data [63] indicate an angle of approximately 45° degrees between the NO molecule axis and the surface normal. The desorption yield shows a linear dependence on the laser fluency [7] indicating a single photon process.

When measuring the state resolved velocity distributions of NO desorbed from a thin NiO(100) film supported by a Ni(100) single-crystal surface with nanosecond laser pulses of 193 nm wave length, corresponding to photon energies of 6.42 eV, Mull et al. observed a bimodality in the velocity distributions [61], as shown in figure 4.1.

There where also some two pulse correlation experiments using femtosecond laser pulses which showed interesting results see figure 4.2 and [66]. First, the desorption yield showed a negative correlation for the vibrational ground state. Second, for the third vibrational state the desorption probability was still enhanced for delay times up to 60 picoseconds, indicating a rather long-lived state. These experiments were performed using a femtosecond laser with wave length 314 nm, corresponding to photon energies of 3.95 eV, and a pulse duration of 550 fs. The two pulses were generated by splitting the original pulse into the s and the p polarised component. The desorption probabilities for different vibrational states as a function of delay time between the two laser pulses are shown in figure 4.2. Negative delay times correspond to the s-pulse preceding the p-pulse.

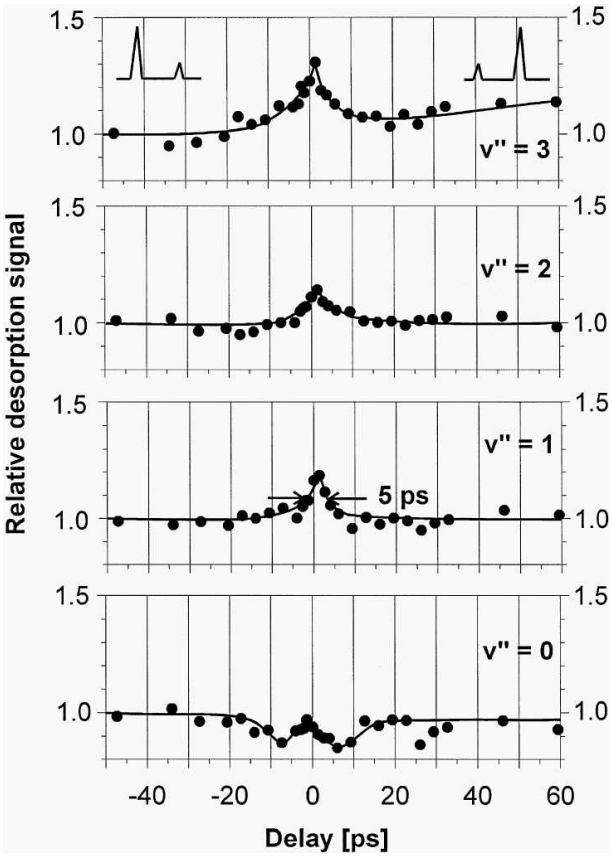

Figure 4.2: The results from the two pulse correlation experiments from [66]. The normalised desorption probability is shown for different vibrational states as a function of delay time between the two laser pulses.

4.2 Potentials

In our simulations we used potential energy surfaces based on two two-dimensional potentials obtained by Klüner et al. [2, 67]. These potential are analytical expressions fitted to energies from ab initio complete active space self-consistent field and configuration interaction calculations. The system calculated consisted of a NiO_5^{-8}-cluster within a semi-infinite crystal of ± 2 point charges and the NO molecule. The two degrees of freedom used are the molecule surface distance Z and the polar angle θ, see figure 4.5. One potential is representing the electronic ground state and the other a set of charge transfer states where an electron from the substrate is transfered into an adsorbate state. The different charge transfer states have similar shaped energy surfaces and thus were merged into one potential [67].

In the ground state the NO molecule is adsorbed to the NiO surface above an Ni atom with the nitrogen atom down and a binding energy of 0.52 eV. It is also tilted away from the surface normal by 45 degrees towards the oxygen atom, compare also the contour plot of the ground state potential in figure 4.3. The ground state minimum is located 2.94 Å away from the surface.

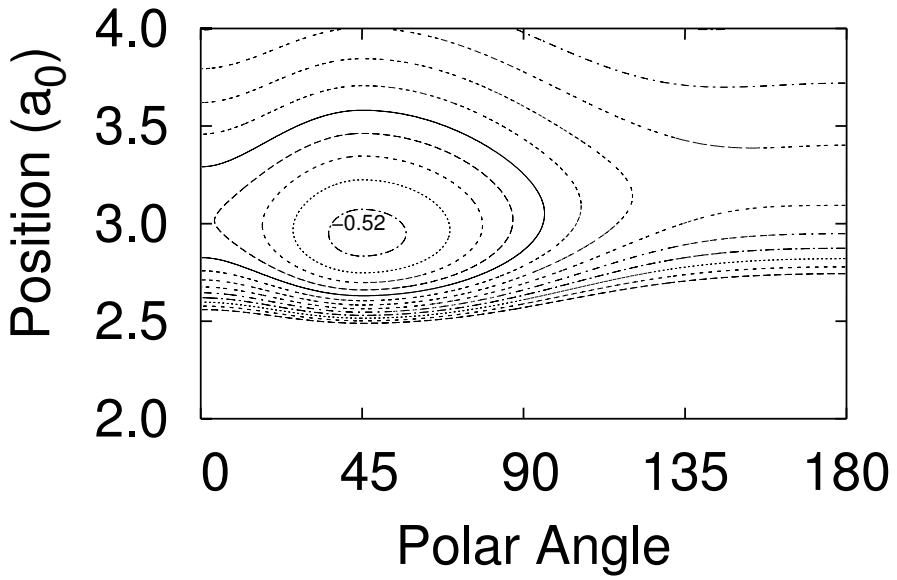

Figure 4.3: The ab initio ground state potential as a function of the centre of mass distance from the surface and the polar angle of the molecule axis. Contour lines are at every 0.04eV between zero and −0.52eV.

The more interesting potential is that of the excited state. It was constructed from a series of similar charge transfer states. As can be seen in figure 4.4 one minimum of the charge transfer state is closer to the surface and at an upright position. Based on the wave packet calculations it was proposed that the bimodality is a consequence of a bifurcation of the wave packet due to the topology of the excited state potential energy surface [3], where when moving closer to the surface one part of the wave packet is deflected along the angular coordinate to smaller angles and gaining a large rotational momentum while the other part moves more directly towards the surface and ultimately gains more translational momentum. As we will show later the wave packet simulations neglected a slow moving late desorbing species, which strongly affects the velocity distributions.

4.2.1 Extension to Higher Dimensions

The NO molecule in front of the NiO surface has a total of six degrees of freedom. Thus for a complete description we needed to extend the ab initio two dimensional potentials. Since there are no full dimensional ab initio results available we were forced to use a model potential to include the additional degrees of freedom. The particular choice of the parameters has to be considered as an educated guess. We like to point out, however, that the qualitative results we obtained did not depend very sensitively on the particular choice of parameters. The complete potential consists of four parts, the original ab initio potential $V_{\mathrm{a}i}$, a corrugation part V_{cor}, the azimuthal variation V_{az} and the intra molecular potential V_{NO}.

$$V^s_{6D}(X,Y,Z,r,\theta,\phi) = V^s_{\mathrm{a}i}(Z,\theta) + V_{cor}(X,Y,Z) + V_{az}(X,Y,Z,\phi) + V^s_{NO}(r)$$

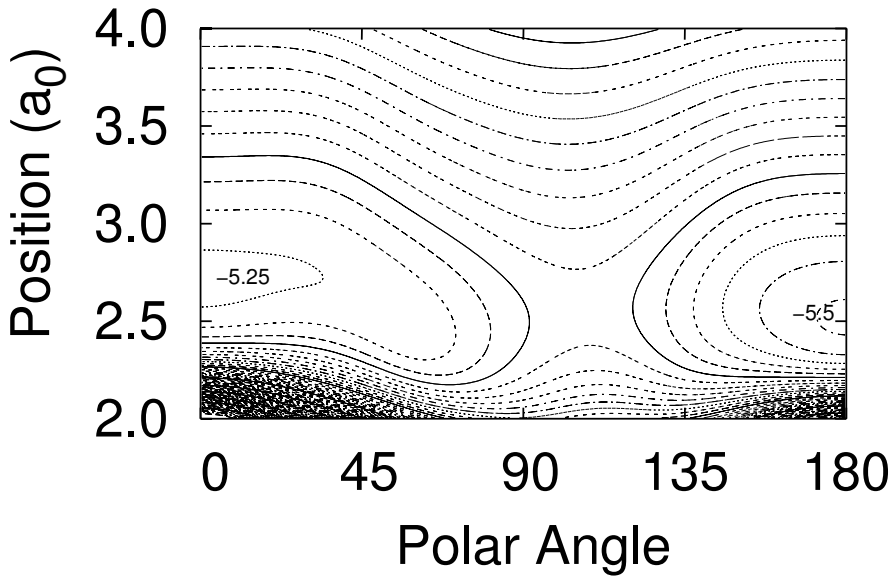

Figure 4.4: The potential energy surface use for the electron transfer state in the NO/NiO system. Contour lines start at −5.5eV and are at every 0.125eV.

The upper index s stand for is either g or e, denoting the ground or the excited state. We assume no difference in the corrugational and azimuthal potential between the adsorbate ground and excited state. The lateral position on the surface is given by the X and Y coordinate while ϕ is the azimuthal angle measured from the X axis and r is the intramolecular N–O distance, compare figure 4.5. The X axis is along the [011] direction and Y is pointing in the $[0\bar{1}1]$ direction, see figure 4.6. For the corrugation potential V_{cor} we used

$$V_{cor}(X,Y,Z) = \frac{C_{cor}}{4} e^{-\lambda_{cor}(Z-Z_0)} \left(2 - \cos G_X X - \cos G_Y Y\right), \tag{4.1}$$

and the azimuthal dependence is given by

$$V_{az}(X,Y,Z,\theta,\phi) = \frac{C_{az}}{2} e^{-\lambda_{az}(Z-Z_0)} \cos 2\phi \sin\theta \left(\cos G_X X - \cos G_Y Y\right). \tag{4.2}$$

In that form the azimuthal potential actually is zero above the Ni atoms, and everywhere else has a period of π in ϕ corresponding to a molecule with identical atoms which should be sufficient as a first approximation. For the strength of the corrugation we choose $C_{cor} = 1.0$ eV and for the azimuthal dependence C_{az} was set to 0.25 eV with equal decay lengths of $\lambda_{cor} = \lambda_{az} = \frac{1}{2}$ Å^{-1}. The lattice constants G_X and G_Y are set to the Ni–Ni distance of the NiO(100) surface $G_X = G_Y = 2.942$ Å as used in [2].

The NO-potential is modelled by a Morse-Potential with different parameters for the ground and the excited state.

$$V^s_{NO}(r) = C^s_{NO} \left(1 - e^{-\alpha_s(r-r_s)}\right)^2 \tag{4.3}$$

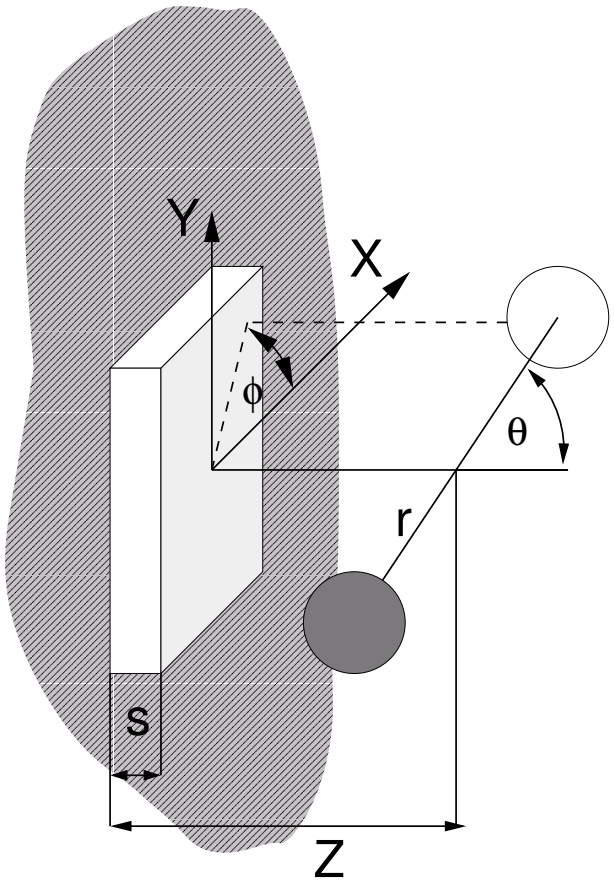

Figure 4.5: This sketch illustrates the coordinate system used for the potential energy surface of the NO in front of the NiO(100) surface, the gray shaded area, together with the surface oscillator, depicted as a square protruding from the surface. X and Y give the lateral position of the centre of mass above the surface while Z denotes the distance from the surface. The X axis is along the [011] direction and Y is pointing in the $[0\bar{1}1]$ direction. The polar angle is given by θ and the azimuth by ϕ. The surface oscillator coordinate is s and r is the intra molecular distance.

The parameters used for the N-O potential were $C^g_{NO} = 6.5$ eV, $\alpha_g = 1.68$ Å^{-1} and $r_g = 2.175$ a$_0$ $= 1.151$ Å in the ground state and $C^e_{NO} = 4.5$ eV, $\alpha_g = 1.50$ Å^{-1} and $r_e = 2.225$ a$_0$ $= 1.177$ Å in the excited state. The equilibrium distances are in accordance with [68] and the binding energy are taken from [56]. But the α's were chosen erroneously, resulting in to low vibrational energies, 143 meV instead of 236 meV in the ground state and in th excited state 106 meV instead of 183 meV. But still, as we will show later, the vibration is decoupled from all the other degrees of freedom and thus the effect of the wrong α-parameters on most of our findings should be small.

Since at 30 amu the mass of the NO molecule is comparable to the mass of the surfaces atoms with 58 amu for the nickel and 16 amu for the oxygen, we wanted to include recoil effects. For that reason, we also included a surface oscillator with coordinate s by directly coupling a harmonic potential to the desorption coordinate

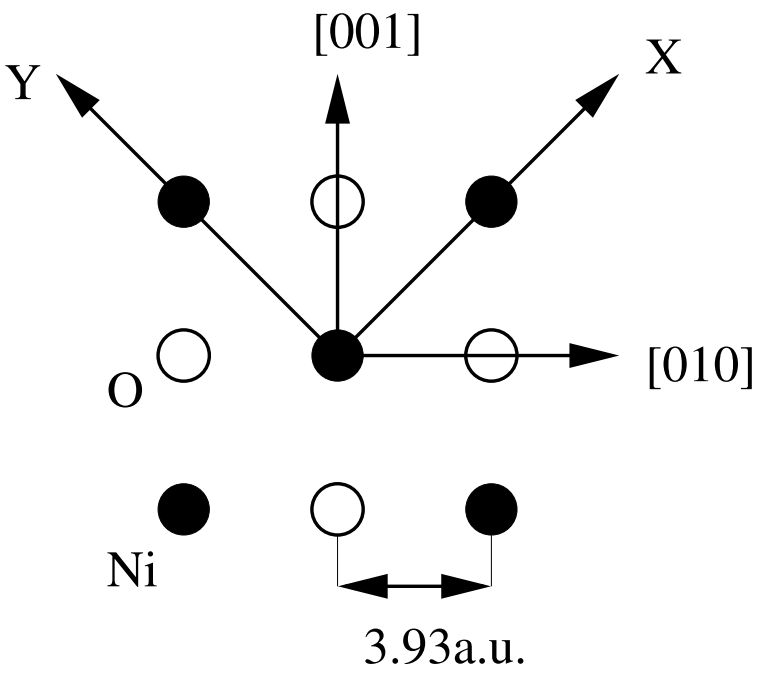

Figure 4.6: Top view of the NiO(100) surface. Filled circles represent nickel atoms and open circles the oxygen. The Ni-O distance is $3.93a.u. = 2.08\mathring{A}$ [67].

which in our case is the distance from the surface Z

$$V^s_{\mathrm{N}+osc}(s, Z, R) = V^s_{\mathrm{N}}(Z - s, R) + V_{\mathrm{osc}}(s)$$

where R denotes all other coordinates. The mass of the oscillator was taken equal to the mass of a Ni atom (58 amu) since NO is adsorbed on top of a Ni atom. According to the usual surface oscillator model [69], the oscillator frequency has been chosen to correspond to the average value of a Debye spectrum. The Debye temperature of NiO has been estimated to be between 500 and 600 K [70]. Accordingly, we have set the oscillator frequency to $\hbar\omega = 27$ meV. The particular value is only of minor importance since the effect of the surface oscillator on the desorption dynamics does not depend very sensitive on the frequency chosen.

Before we come to the discussion of our results a quick note on the nomenclature used, by oscillator we will refer to the surface oscillator and the intra-molecular oscillations of the NO molecule will be termed vibrations.

4.3 Mixed Quantum-Classical Results

Based on the potentials presented in the previous section we simulated the NO desorption from the NiO(100) surface using surface hopping with an optical potential. As the collective state we use the ground state and only the charge transfer state is treated explicitly. As mentioned before, in this case no electronic Schrödinger equation must be integrated.

4.3.1 Procedure

The simulation procedure is basically the same as outlined in the fewest switches section. We usually start our trajectories in the excited state where they move classically for a certain time. After a Franck-Condon transition the movement of the molecule is continued on the ground state potential for a maximum propagation time or until it reaches a certain distance Z_{Cutoff} from the surface and is considered desorbed. In most of our simulations we used 12.1 ps as maximal propagation time. Trajectories with a total energy below zero after the last de-excitation into the ground state are stopped immediately, since they can not desorb.

The time spent in the excited state, the residence time, is determined by the optical potential. After each integration step, with length dt, in the excited state we calculate the optical potential Δ at the current position R and if the decay probability $p = \frac{2\Delta(R)}{\hbar}dt$ is larger than a uniformly distributed random number between 0 and 1 we jump into the the ground state, otherwise we continue in the excited state. Simulating the excitation process via an optical potential is straight forward.

For constant optical potential this procedure is equivalent to the Gadzuk scheme [71], as used in [61]. In the Gadzuk scheme the residence times are kept fixed and the overall result is obtained by averaging over different residence times with weight function $w_\tau(t) = \frac{1}{\tau}\exp(-t/\tau)$, where the average residence time or resonance lifetime τ is an adjustable parameter directly connected to the strength of the optical potential via

$$\tau = \frac{\hbar}{2\Delta}. \tag{4.4}$$

All the results shown are averaged over at least 10^5 trajectories, resulting in an accuracy of roughly $\sqrt{10^{-5}} \approx 0.003$. If we look at state resolved results as in figure 4.13 or 4.16 we used 10^6 trajectories corresponding to $\sqrt{10^{-6}} = 0.001$.

The trajectories are started around the position of the ground state minimum assuming a Gaussian distribution in position and momentum according to the curvature of the ground state potential energy surface. This corresponds to a harmonic approximation for the potential at the minimum position. In principle the distributions should be given by the Wigner distribution function corresponding to the true ground state wave function according to equation (2.91), but the masses of the nuclei are rather large compared with $\hbar$ and since we do not know the exact ground state wave function we use this approximation.

To check on the reliability of the harmonic approximation we performed a series of test calculations, in the two dimensional model using only the distance from the surface Z and the polar angle θ and in the full seven dimensional model. All these test were done by averaging over one hundred thousand trajectories. If the harmonic approximation is a good one the initial momentum and position distributions would be stationary when propagated along time and consequently the desorption probability would not change. Thus we did not start the simulation in the excited state but in the ground state and only after a certain offset time t_O we switched into the excited state and continued then as normal. Unfortunately the desorption probability changed significantly with the offset time (see figure 4.7), mainly due to a spreading in the position distribution.

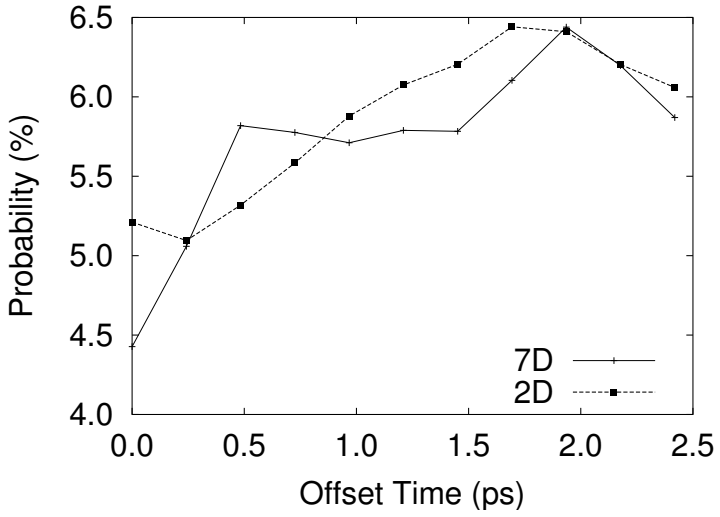

Figure 4.7: This figure shows the desorption probability in the two and seven dimensional model as a function of the offset time spent in the ground state prior the initial excitation.

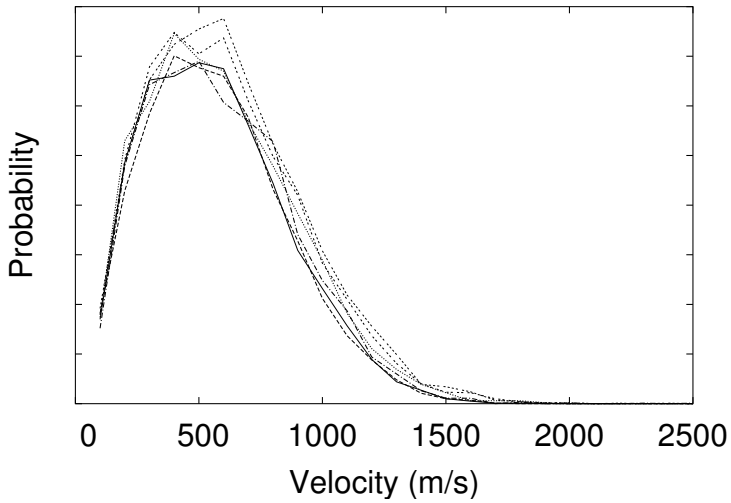

Figure 4.8: The velocity distribution of the desorbed molecules in the two dimensional model for different offset times up to 1.2 ps.

However, the desorption probability is not such a significant number as it first seems. It can not be compared directly to the experimentally measured desorption yields, since we do not know the excitation probability included in the experimental results. For that reason the main focus of this work is on the momentum distributions of the desorbed molecules rather than the desorption probability itself. Thus we compared the velocity, rotational momentum and for the full dimensional case also the vibrational state and oscillator state distributions. As can be seen for the velocity distribution in figures 4.8 and 4.9 the shape of the various distributions hardly changes with the offset time.

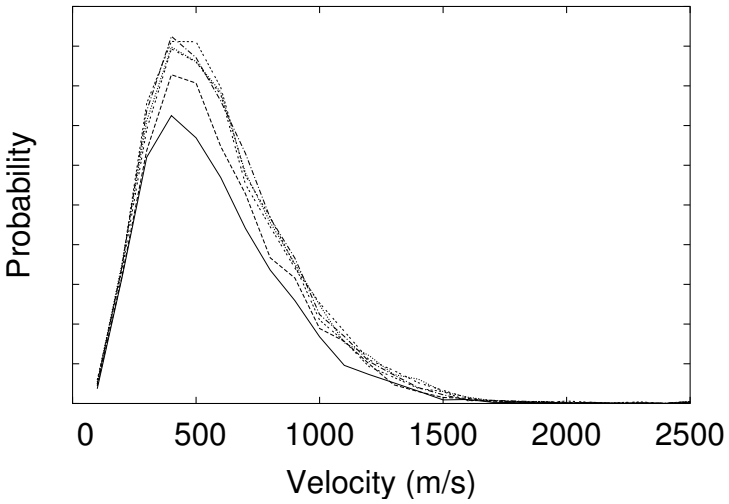

Figure 4.9: The same as in figure 4.8 but for a model using all seven degrees of freedom.

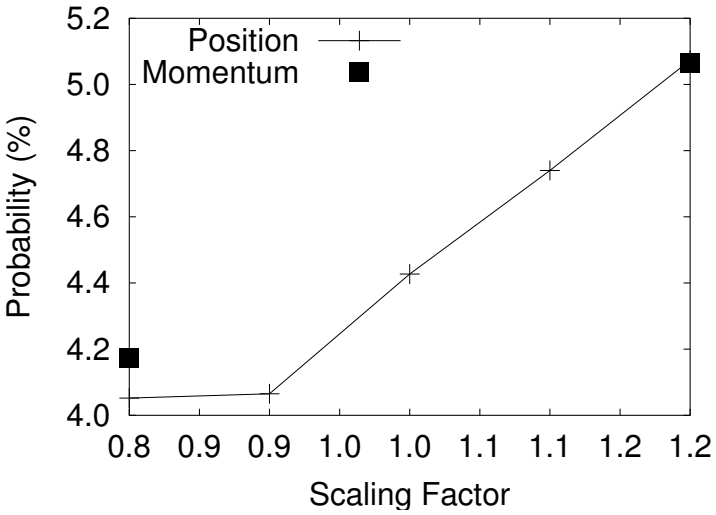

Figure 4.10: Here we show the dependence of the desorption probability for the seven dimensional model as a function of the scaling factor of the initial width for the position and momentum distributions. (Note that for the momentum width we show only two values.)

Note, that the different peak heights are mainly a result of the different desorption probabilities.

We also performed another test by directly scaling the width of the initial position respectively momentum distribution, in the seven dimensional model. The influence on the desorption probability is of the same magnitude as for the previous test, compare figure 4.10, where narrower distributions lead to smaller desorption probabilities, as could be expected due to the discussion of the previous chapter. But again the shape of the distributions of the desorbed trajectories showed no significant dependency on

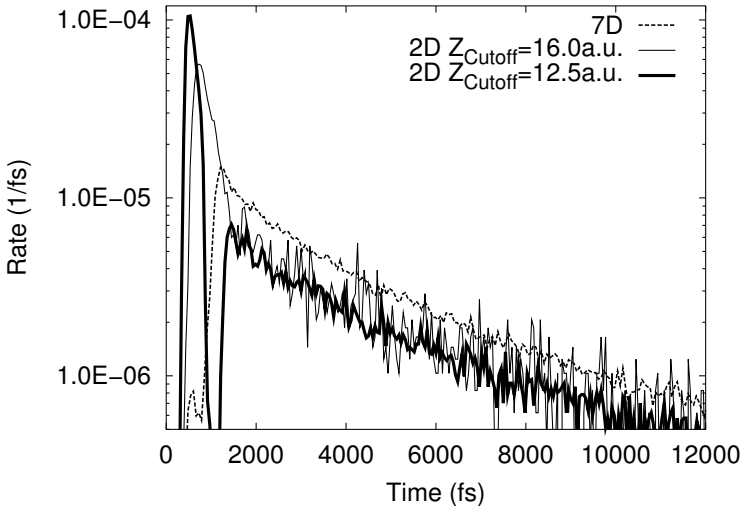

Figure 4.11: Desorption rate as a function of time (excitation at time $t = 0$) in the two-dimensional (solid lines) and the seven-dimensional simulations (dashed line). The 2D results have been obtained with a cutoff distance of $Z_{Cutoff} = 12.5$ a.u.(thick solid line) and 16.0 a.u. (thin solid line) while in the 7D calculations $Z_{Cutoff} = 16.0$ a.u. was chosen.

the initial width. Consequently for all our simulations we used the normal distributed initial position and momenta.

4.3.2 Comparison with Wave Packet

We started our investigations with a simulation restricted to the Z and the θ coordinates of the ab initio potential to be able to compare our result against the wave packet calculations from Klüner et al. [3] and by this means validating the use of classical mechanics for the motion of the nuclear coordinates. We also employed the Gadzuk scheme and used a lifetime of 24.19 fs (= 1000 a.u. as in [3]) together with a cutoff distance of 12.5 a_0[1] corresponding to the onset of the transfer function used in the wave packet calculations [67]. For that lifetime the wave packet calculations resulted in a desorption yield of 3.3% whereas the classical simulations lead to 4.8%. This was puzzling since normally we would have expected the wave packet results to give a higher yield due to desorption from classically forbidden tails of the wave function. Closer examination of the desorption rate, i.e. the probability of a trajectory to pass the cutoff distance per unit time, as a function of time helped to resolve this discrepancy, see figure 4.11. We found there to be two kinds of desorbing trajectories, those desorbing within the first 1.2 picoseconds, which we will call early and a long trail of late desorbing trajectories. The wave packet results were obtained by propagating in the ground state until the desorption yield saturated, this was the case after

[1]The calculations were done using atomic units (a.u.) as a unit system. The unit length in that system is set to a Bohr radius $a_0 = 0.5291772$ Å[55], the unit energy is one Hartree (27.21 eV) which, together with $\hbar$ set to one, is leading to a unit time of 0.02419 fs.

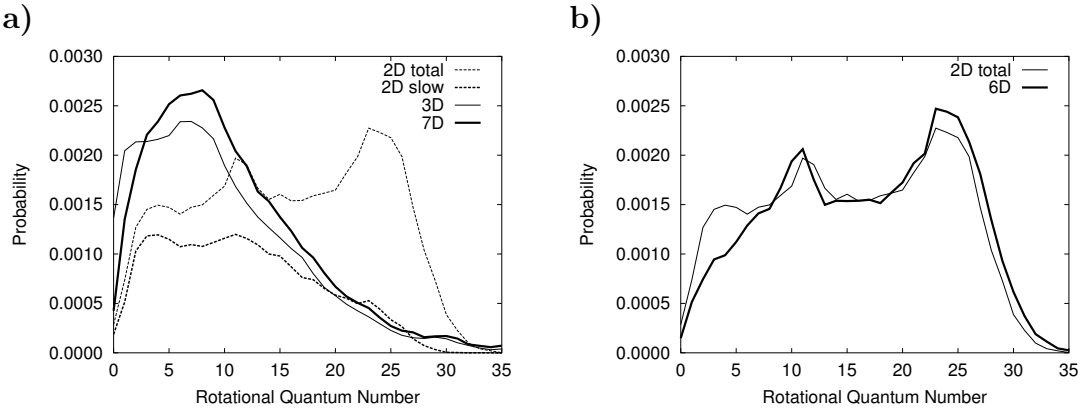

Figure 4.12: Comparison of the rotational momentum distributions of the desorbed molecules for all the models considered in our simulations.

1.2 ps. Note that for the 2D results, with cutoff distance 12.5 a_0, there is a gap in the desorption probability at that time. If in our simulations we consider only the early desorbing trajectories the desorption probability goes down to 2.91% which is in much better agreement with the wave packet results. When increasing the cutoff distances naturally the early desorption probability goes down (2.49% for 16.0 a_0 and 1.56% for 20.0 a_0) and also the gap in the desorption flux vanishes, compare figure 4.11 where we plotted the desorption rate for a cutoff distance of 16.0 a_0 as well. The total desorption probability naturally does not depend on the cutoff distances. When not comparing to the wave packet results we will use a cutoff distance of 16.0 a_0 since at 12.5 a_0 the binding energy is still 10 meV. Note that for our method the computational cost in increasing the cutoff distance is small.

The existence of an early and late desorbing species of molecules can be understood by a closer examination of single trajectories and by taking the position of the potential energy surface minima into account. In the ground state minimum the NO molecule is tilted from the surface normal by 45 degrees. In the excited state one minimum is an upright position closer to the surface. Thus after the excitation the molecule is accelerated towards the surface and into a more upright position. With a lifetime of $24.19fs$ as used in our simulations most molecules relax to the ground state before they reach the excited state minimum. After the transition back on the ground state the molecules hit the repulsive potential wall and are either scattered directly into the vacuum, resulting in the early desorbing species, or they start to rotate in front of the surface. Those can either be trapped dynamically for very long times or desorb after only a few rotations, leading to the late species. The molecules that are scattered directly into the vacuum have a higher translational and rotational momentum as the late desorbing molecules. The difference in the rotational momentum distribution between the late and the early trajectories can be seen in panel a) of figure 4.12 where for the two dimensional case we plotted the distributions for all and the late trajectories only. The late molecules show a broad peak between $J = 3$ and 11 and fall off for higher momenta. The early species shows a large peak at $J = 25$ and a smaller one at $J = 12$. Note that for a free rotating NO molecule the rotational period T is connected

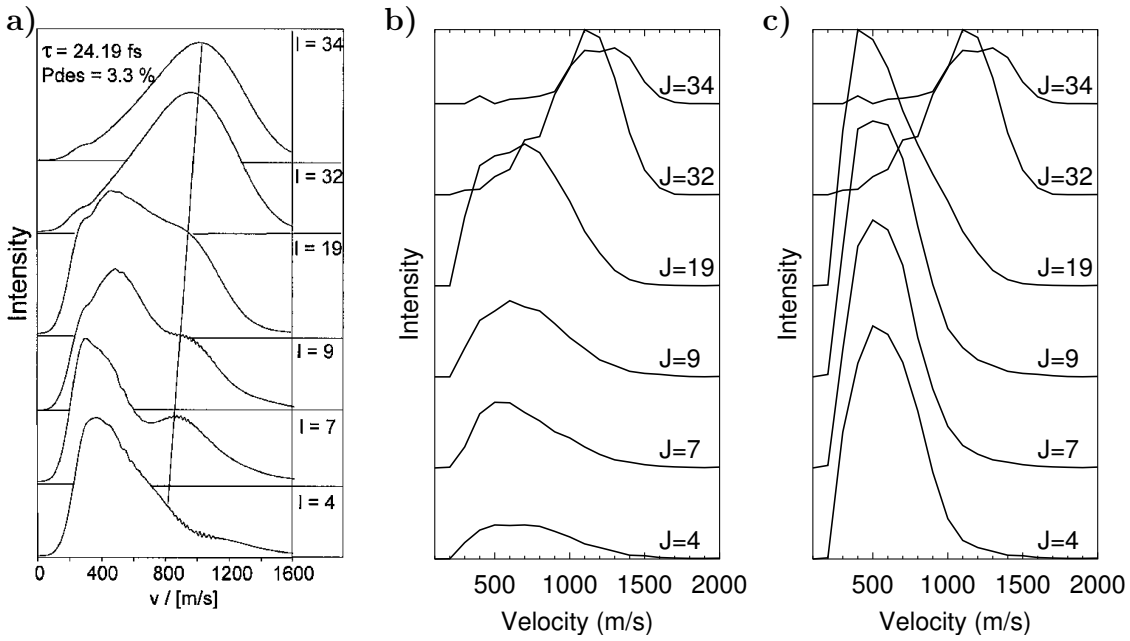

Figure 4.13: The NO velocity distribution of the desorbed molecules for selected rotational states, a) from wave packet calculations from [3] and our two dimensional simulations with $Z_{Cutoff} = 12.5$ a.u. and the Gadzuk scheme once for the early desorb panel b) and for all desorbed trajectories panel c).

to the rotational quantum number J via $T = \frac{2\pi\theta}{\hbar}\frac{1}{J}$, where $\frac{2\pi\theta}{\hbar}$ is equal to 9.79 ps. Thermalisation will eventually lead to the suppression of the late desorption but on a much larger timescale of several picoseconds (the total time scale of our simulation is twelve picoseconds), we will discuss the influence of friction in the oscillator coordinate in section 4.6.

As we can see in figure 4.13 there is good qualitative agreement between the velocity distributions of the early desorbing classical trajectories and the wave packet results from reference [3]. Both show wide peaks at similar velocities that shift to the right for larger rotational momenta. Note, that the peak shift was also observed experimentally. The bimodality is hinted in the wave packet distributions and is less apparent in our results. However, when also considering the late trajectories the shape of the momentum distributions changes considerably and only for the highest rotational states, which are dominated by the early trajectories, the agreement with the wave packet simulation remains.

In addition we also compared the desorption probability as a function of residence time, as shown in figure 4.14. We find the same offset and peak position as it was found with the wave packet simulations [67]. Interestingly the minimum residence time necessary for desorption is with 40 fs rather large, thus the desorption probability will depend strongly on the excited state lifetime. The desorption probability as a function of residence time also shows the same oscillatory behaviour already found in the Antoniewicz like simple model, compare figure 3.8.

We also compared the Gadzuk-Scheme for relaxation into the ground state with

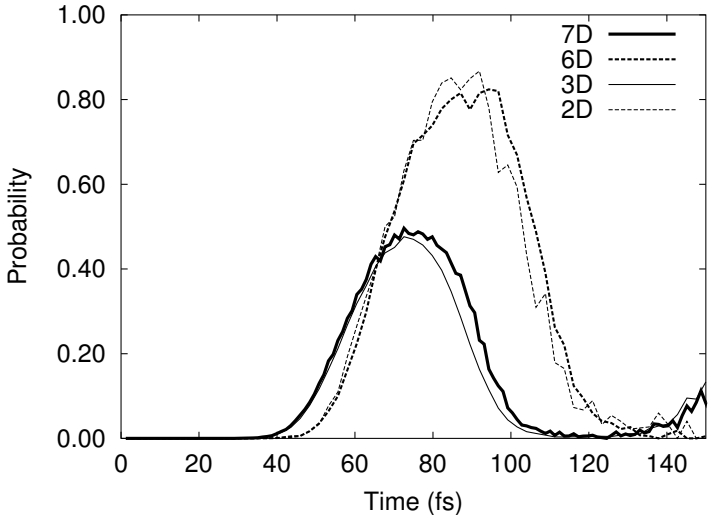

Figure 4.14: The desorption probability as a function of the residence time for the 2D, 3D, 6D and 7D model.

decay using an either constant or exponentially decreasing optical potential. The mean lifetime τ and the strength of the optical potential Δ_0 are related via

$$\Delta_0 = \frac{\hbar}{2\tau} \tag{4.5}$$

and the spatial dependence of optical potential is given by

$$V_{opt} = V_{opt}(Z) = \Delta_0 e^{-\gamma(Z-Z_0)} \tag{4.6}$$

Z_0 is the ground state equilibrium distance of the NO molecule from the surface. A zero inverse decay length γ corresponds to a constant V_{opt}. Using an exponentially decaying optical potential is motivated by the fact that the coupling between the ground and the charge transfer state is given by the overlap of the molecular orbital with the bulk electrons. As expected we found no difference between the constant optical potential and the Gadzuk-Scheme, neither for the desorption probability nor the momentum distributions. More surprising was that switching on the exponential decrease of the optical potential had basically no effect on the velocity distributions and only changed the total desorption probability. For all further simulations we used a constant optical potential, except of course, the discussion of localised optical potentials in section 4.7.

4.4 Influence of Vibration

In order to study the influence of additional degrees of freedom on the desorption process, we extended the potential energy surface to seven dimensions by considering the remaining NO degrees of freedom and one surface oscillator coordinate according to equations (4.1), (4.2) and (4.3). We start our high-dimensional treatment

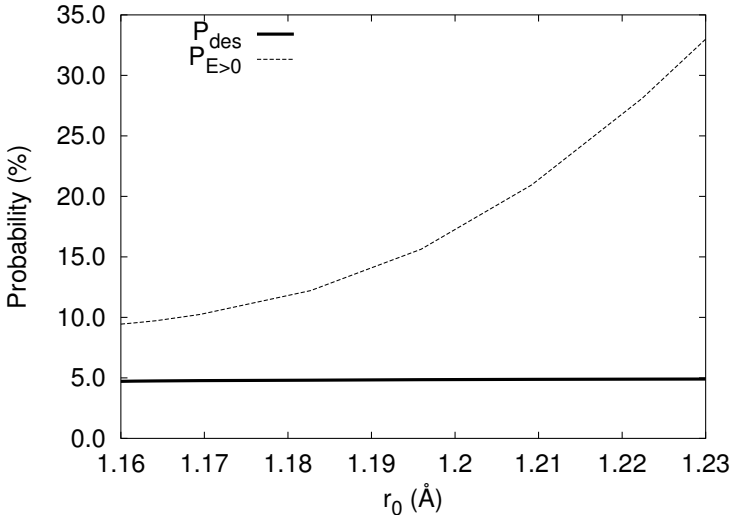

Figure 4.15: Desorption probability and the probability for total energy to be larger than zero as a function of the N-O equilibrium distance in the charge transfer state.

with an analysation of the vibrational population of desorbing molecules. It is well-known [6, 68], that using the gas phase value of $r_{NO^-} = 2.377$ $a_0 = 1.258$ Å for the NO^- ion equilibrium distance [56] leads to unrealistic high vibrational excitations. The relative vibrational populations P_v/P_0 of the vibrationally excited states characterised by the vibrational quantum number v are much larger than the ones derived from the experiment [7, 64, 65]. This behaviour is reproduced in our simulations.

However, above the ionised NiO(100) surface the strong electrostatic field reduces the elongation of the N-O bond of the NO^- anion according to quantum chemical calculations [68]. The anion bond is only extended by 0.05 $a_0 = 0.026$ Å compared to the neutral NO molecule above the NiO(100) surface instead of 0.2 a_0 as in the gas phase. Consequently, we have used a N-O bond distance of $r_g = 2.225$ $a_0 = 1.177$ Å for the NO^- anion in the excited state. The vibrational population resulting from simulations with the new NO equilibrium distance are much closer to the experiment. We also observed that including the surface oscillator had no effect on the vibrational distribution.

Furthermore, when varying the NO^- equilibrium distance we observed that the total desorption probability did not change within the level of the accuracy of our simulations. This is illustrated in figure 4.15, where we plotted the desorption probability, without the surface oscillator, as a function of the NO^- equilibrium bond length. Also shown is the fraction of trajectories with positive total energy. Despite the increasing number of trajectories with sufficient energy for desorption the actual desorption probability remains constant. This indicates that energy transfer from the vibrational coordinate into other degrees of freedom is very low. This is further confirmed by the fact that not only the desorption probability hardly changes with r_{NO^-} but also the momentum and rotational momentum distributions do not vary. Thus we conclude, that our unfortunate choice of potential widths α for the NO potential has no effect

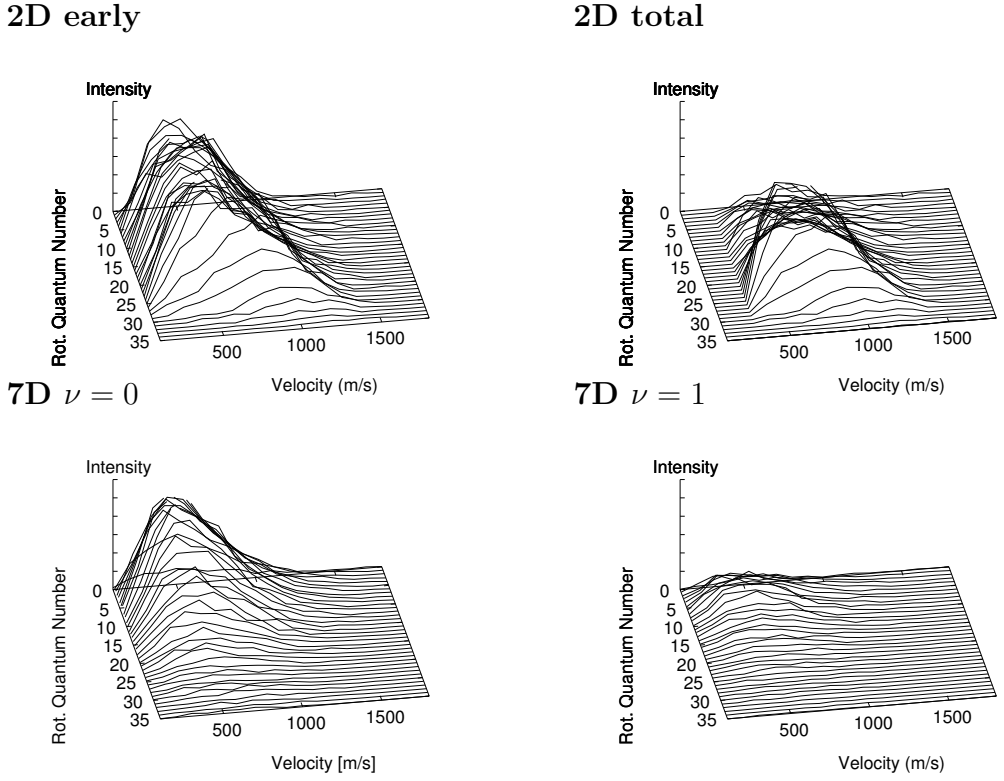

Figure 4.16: Velocity distributions as a function of the rotational state for the early (top) and all (bottom) desorbing molecules in the two dimensional simulation and for the first two intra molecular vibrational states in the seven dimensional model. (Note the intensity scales are all the same.)

on our other findings.

4.5 Non-Rigid Surface

Since the mass of the substrate atoms and that of the NO molecule are comparable, recoil processes during the desorption reaction are likely to occur. In order to include energy transfer to the substrate in the simulations, we have coupled the 2D and 6D potentials to a surface oscillator with realistic parameters, as described in section 4.2.1,

	2D	3D	6D	7D
z_{CO} (a_0)	12.5	16.0	16.0	16.0
P_{des} (%)	4.84	3.63	4.74	4.02
P_{early} (%)	2.93	0.32	2.53	0.32
E_{rot} (K)	770	366	883	395

Table 4.1: Desorption probabilities and mean rotational energies according to the 2D, 3D, 6D and 7D calculations. Early means desorption within the first 1.2 picoseconds.

at negligible computational cost.

In table 4.1 we have collected the main results with respect to the desorption probability and the rotational temperature of desorbing molecules according to the 2D, 3D, 6D and 7D calculations. Going from 2D to 6D, i.e. including the remaining molecular degrees of freedom in the simulations, has only a small influence on the desorption dynamics. The same is also true for the transition from 3D to 7D. This can be seen for the rotational momentum distributions in figure 4.12 and in figure 4.14 for the desorption probability as a function of residence time.

However, including recoil processes of the substrate, by coupling the motion of the adsorbate molecule to a surface oscillator, changes the outcome of the trajectory calculations significantly. While the total desorption probability is only reduced by about 1%, the effect on the early desorption channel is really dramatic: It is reduced by a factor of eight. This also manifests itself in the desorption rate as a function of time, depicted in Fig. 4.11, where the initial "early" peak is basically absent in the 7D results. But the most dramatic effect of the surface oscillator is on the rotational momentum distribution. While in the 2D calculations we obtain a double peaked structure with a large probability for high rotational quantum numbers, the inclusion of the surface oscillator causes the suppression of the peak at high J. The shape of the distribution is now similar to that of the late molecules in the rigid surface case. This is leading to a greatly reduced mean rotational energy of the desorbing molecules, 366 K and 395 K for 3D and 7D calculations, respectively, instead of 770 K for the 2D and 883 K for the 6D calculations. These reduced rotational temperatures are in fact in much better agreement with experiment [61].

As far as the vibrational population in desorption is concerned, it is hardly influenced by going from six to seven dimensions. Also the shape of the velocity distributions for different rotational momenta do not depend on the vibrational state. See figure 4.16 where we show the 7D results for the first two vibrational states. This indicates that the vibrational dynamics is efficiently decoupled from the remaining degrees of freedoms due to the fact that it corresponds to the shortest time-scale in the molecular dynamics.

As far as the comparison between experiment and theory with respect to the velocity distribution is concerned, however, the agreement was already greatly reduced by taking the late desorption channel into account as shown in figure 4.13. Including all the other degrees of freedom, especially the surface oscillator, further reduce the bimodality in the velocity distributions.

In Fig. 4.16, we compare the velocity distribution according to the 7D with those of the 2D calculations. The velocity distribution for the 3D simulation is rather similar as the 7D whereas the 6D results compare well to the 2D distribution. There is no indication of any bimodal velocity distribution in the seven dimensional results which was found in the experiment [61] and which was also reproduced in the wave packet calculations [3]. Note that apart from an overall scaling due to the reduced desorption probability the shapes of the velocity distributions summed over all rotational momenta are almost identical for all dimensionalities used.

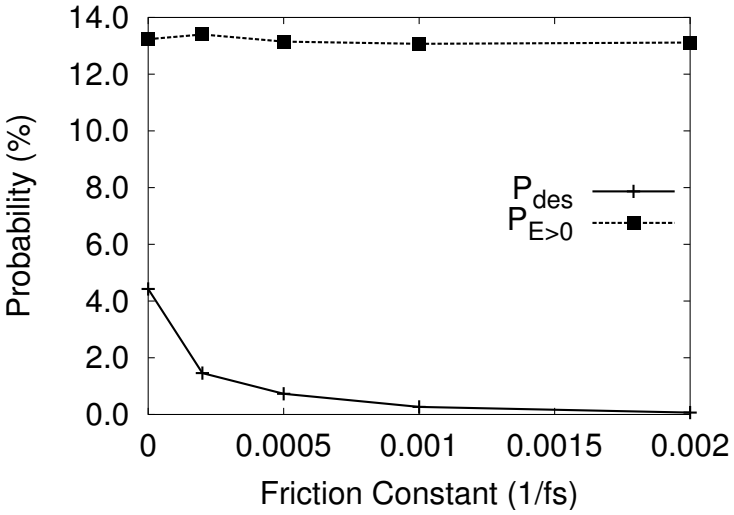

Figure 4.17: The desorption probability and the probability for a trajectory to have a positive total energy, at the time of the transition from the excited into the ground state, as a function of the friction constant γ.

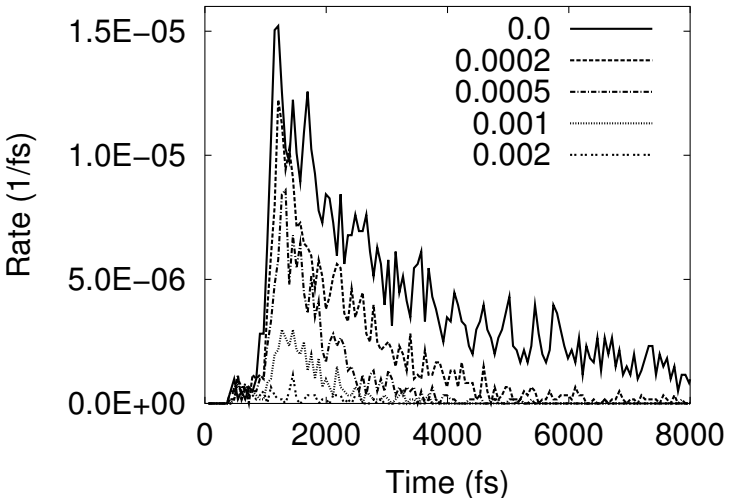

Figure 4.18: The desorption rates as a function of time for different friction constants γ.

4.6 Friction

To investigate the possible effect of dissipation at the surface on the desorption dynamics we added a frictional force term $-m\gamma\dot{s}$ to the surface oscillator in the full dimensional model, i.e. if $\ddot{s} = F_s(R)$ was the original equation of motion with the force $F_s(R)$ and R standing for all the coordinates the new equation of motion is given by

$$\ddot{s} = F_s(R) - m\gamma\dot{s}. \tag{4.7}$$

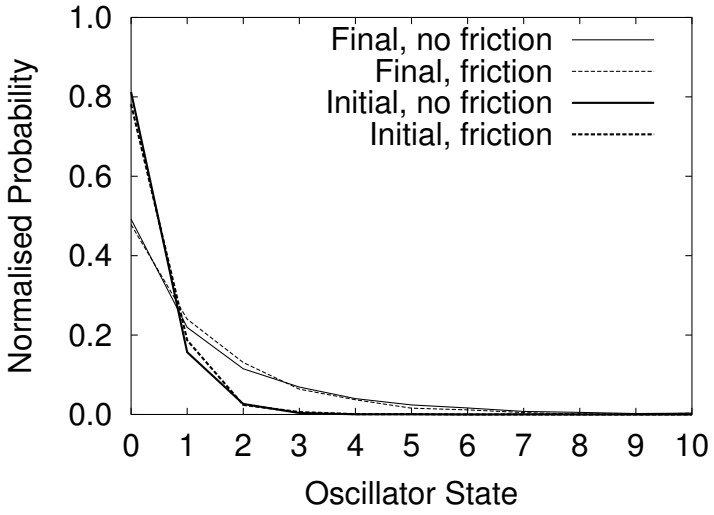

Figure 4.19: The initial and final occupation probabilities of the surface oscillator states for the desorbed molecules with and without friction. The probabilities are weighted with the corresponding inverse desorption probabilities (here $P_{des} = 0.044$ for the case without friction and $P_{des} = 0.0146$ for the case with friction, where the friction constant was $\gamma = 0.0002\frac{1}{fs}$).

If we are not in the aperiodic limit, i.e. if $\gamma < 2\omega$ where ω is the oscillator frequency, the oscillation amplitudes of a free damped oscillator decrease with time as

$$e^{-\frac{\gamma}{2}t} \tag{4.8}$$

and the corresponding decay time τ_D is given by $\tau_D = \frac{2}{\gamma}$. The values used for γ and the corresponding decay times τ_D are shown in table 4.2. We used decay times between 1 ps and 10 ps as we would expect them for phonon mediated energy dissipation. All results shown in this section are averages over 10^5 trajectories thus results are accurate to about 0.3 percent. The influence of the friction on the desorption probability is shown in figure 4.17. We see that already a relatively small friction causes a considerable drop in the desorption probability from 4.4 percent down to 1.5 %. Also shown in fig. 4.17 is the probability of a trajectory to have a positive total energy at the moment of de-excitation. This is basically independent of the friction since the lifetime in the excited state at $24.19fs$ is much shorter than even the shortest τ_D used. Thus all the dissipation take place while the molecule is in it's ground state and only the time during which desorption still takes place is shortened by the friction. This is evident from figure 4.18,

γ [fs^{-1}]	0.0	0.0002	0.0005	0.001	0.002
τ_D [ps]	∞	10.0	4.0	2.0	1.0
P_{des} [%]	4.427	1.459	0.73	0.268	0.067

Table 4.2: Values used for the friction constant γ and corresponding decay times τ_D and desorption probabilities.

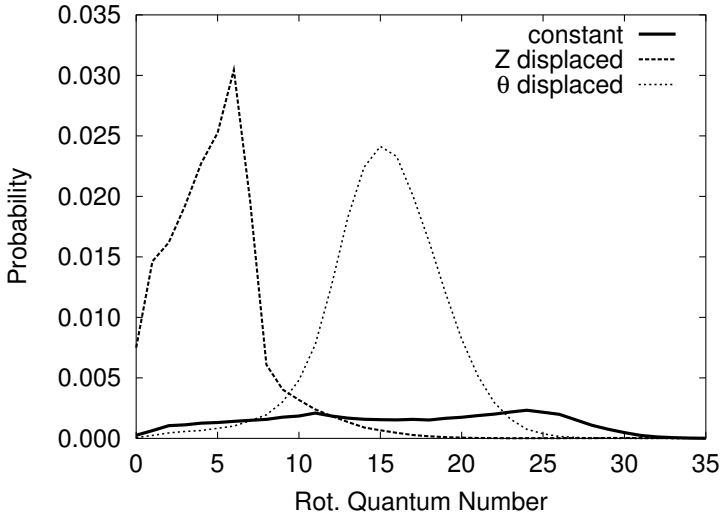

Figure 4.20: Rotational distribution of desorbed molecules for 6D with different optical potential

where we plotted the desorption rate as a function of time (compare also figure 4.11). As we already discussed in a previous section 4.3.2, without friction there is a long trail of molecules desorbing at very large times, which contribute a substantial amount to the total desorption probability. This tail is cut off by the dissipative effects and thus lowering the desorption probability.

The effect of the friction on the momentum distribution and the vibrational, oscillator and rotational state occupation probabilities of the desorbing molecules is negligible, apart from an overall scaling due to the reduced desorption probability. As an example we picked the occupation probability of the oscillator states. In figure 4.19 we compare results with and without friction. We further show the initial and final state distributions of the desorbing trajectories, where with initial we mean at the start of the simulation and final refers to the time of passing the cutoff distance Z_{Cutoff}. All distributions are normalised by scaling with the inverse of the corresponding desorption probability. We see that for desorbing trajectories the surface oscillator gains energy and that there is no significant difference between the distributions for both simulations. For the initial distribution this is what we should expect. However, the agreement for the final distributions it is more surprising. But the explanation is also very simple, since trajectories that do desorb leave the surface at times usually smaller than the corresponding decay time τ_D of the oscillator, the amount of energy lost is rather small and thus the final occupation probabilities are unaffected. Note that apart from numerical inaccuracy due to the smaller number of desorbing trajectories, this is true for all frictional constants used.

	Z displaced	θ displaced
A [eV]	1.36	1.36
Z_0 [Å]	2.54	2.75
σ_Z [Å]	0.1	1.0
θ_0	$\frac{1}{4}\ \pi$	$\frac{2}{3}\ \pi$
σ_θ	$0.1\ \pi$	$0.3\ \pi$

Table 4.3: The parameters used in the simulations with the localised optical potential of equation (4.9).

4.7 Non Constant Optical Potential

The optical potential describes the coupling of the adsorbate states with the substrate states. That coupling is given by the overlap integrals of the adsorbate orbitals with the corresponding substrate orbitals. Thus, one would expect it to be exponentially decreasing with the molecule surface distance. We tried several such potentials with different strength and different decaying length for the six dimensional model but, apart from a change in the total desorption probability, we found no significant influence on the velocity and momentum distributions of the desorbing molecules.

Since we can not exclude the fact that the coupling to the substrate states might be particularly large for certain configurations of the adsorbate we also did some simulations with an optical potential localised in the Z-θ plane. The form of the potential used is given by

$$V_{opt}(Z,\theta) = A \exp\left[-\left(\frac{Z-Z_0}{\sigma_Z}\right)^2 - \left(\frac{\theta-\theta_0}{\sigma_\theta}\right)^2\right], \tag{4.9}$$

and the corresponding parameters are given in table 4.3. In figure 4.20 we plotted the resulting rotational distribution of desorbed molecules and also as a comparison the distribution as obtained with a constant optical potential. We see, that for both cases the distributions are narrower and that for the optical potential located closer to the surface the rotational excitation is decreased while for the potential shifted to larger polar angles the distribution is centred at a rotational momentum of 15 $\hbar$. The effect on the velocity distribution is similar dramatic but these are widened instead. Certainly the parameters used are somewhat extreme but so is the effect on the momentum distributions. These models show that some features of the distributions could be caused a non-constant electronic coupling between the adsorbate and the substrate states.

4.8 Multiple Excitations

As mentioned above, our mixed quantum-classical scheme with optical potential can also be used to describe excitation processes, by introducing an extra optical potential responsible for transitions from the ground state into the excited state. First we will

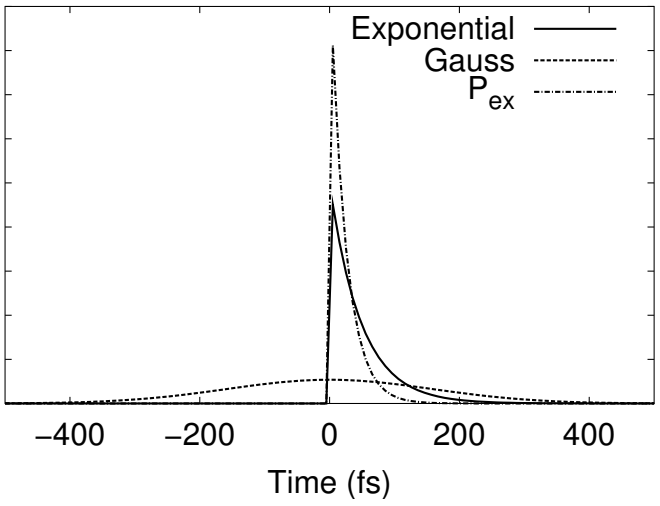

Figure 4.21: The Gaussian and exponential optical potential used for excitation as a function of time. For comparison we also show the probability to be still in the excited state after an excitation at time 0.

investigate the influence of different excitation schemes on the desorption dynamics by using optical potentials with Gaussian, exponential and delta shaped time dependence for the excitation. In a second part we will combine a delta excitation at time zero with Gaussian excitations at different time shifts in an attempt to simulate the time-correlated two-pulse laser desorption experiments of Eichhorn et al. [66].

4.8.1 Initial Excitation

Before simulating two pulse excitations we looked at the influence of the excitation pulse shape on the desorption dynamics. We compare three different scenarios, a single excitation at time zero, corresponding to delta-function like optical potential, an excitation via an exponential decaying optical potential with a time constant twice as long as of the excited state lifetime and a much wider spread Gaussian optical potential with a width of 610 fs. As for the residence lifetime we keep it at 24.19 fs as for all the previous simulations. The Gaussian and the exponential optical potential are plotted

	delta	exponential	Gauß
P_{des} [%]	5.87	8.03	12.96
av. up jumps	1.00	1.50	1.65
av. jumps of des.	1.00	1.74	2.57
E_{tot} of des. [eV]	0.25	0.31	0.48

Table 4.4: Desorption probability, average number of excitations per trajectory and per desorbed trajectory and the mean total energy of the desorbed molecules for the different excitation schemes.

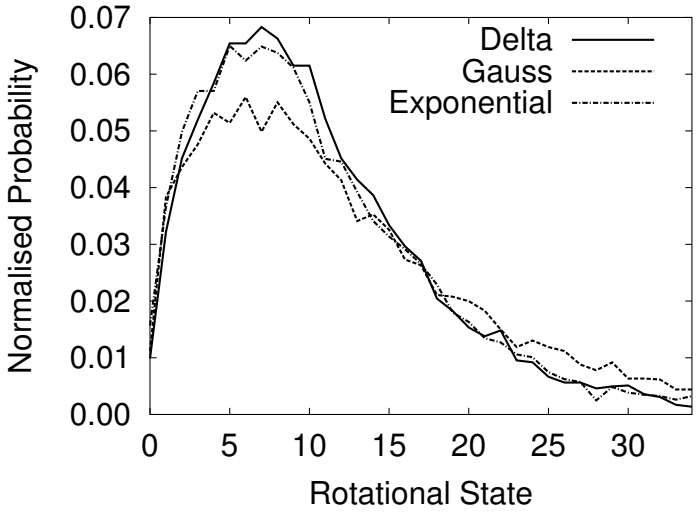

Figure 4.22: The rotational distributions for the different excitation mechanisms weighted with the corresponding inverse desorption probabilities.

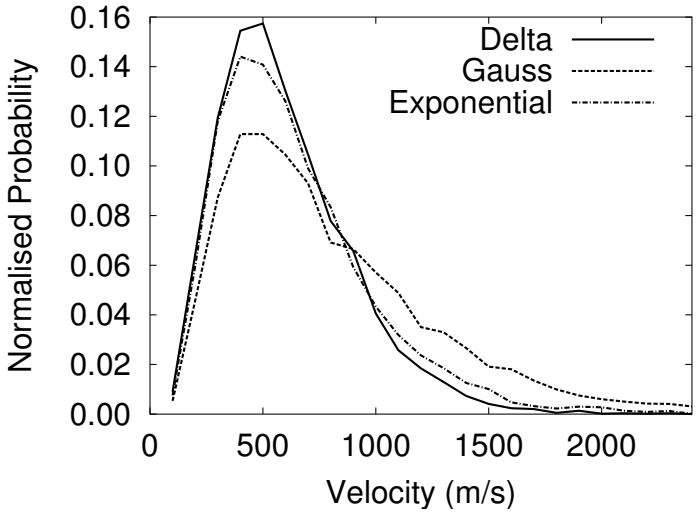

Figure 4.23: The velocity distributions weighted with the inverse desorption probability of the corresponding excitation scheme.

in figure 4.21, where, for comparison, we also plotted the probability to still be in the excited state after a transition at time zero. All simulation runs we propagated in the ground state for sufficient long times before the first excitation could occur and all results are sampled over 10^5 trajectories.

We first notice that the desorption probabilities for the exponential and the Gaussian scheme are higher that for the delta excitation, see table 4.4. This can be connected to the number of excitations per trajectory, for both schemes this was larger than one. The number of excitations per trajectory is connected to the strength of the excitation

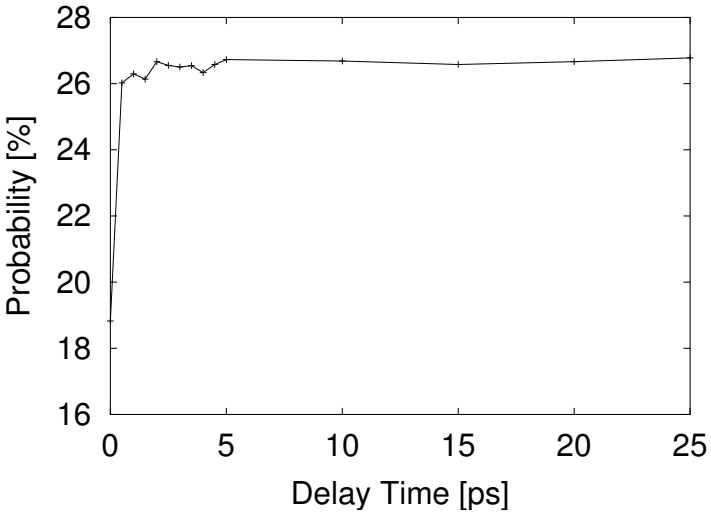

Figure 4.24: The desorption probability for the two-pulse excitation as a function of delay time.

potential, which we deliberately set large enough to result in more than one excitation. If every trajectory would be excited only once or not at all we would not see any effect, apart from an overall scaling in the probabilities for less than one excitation, since all trajectories are independent of each other. The most significant difference between the exponential and the Gaussian scheme is the width in time in comparison with the residence lifetime. The Gaussian scheme is much wider and despite nearly the the same number of excitations per trajectory as for the exponential potential the desorption probability is significantly enhanced. This can be related to the larger probability for two or more excitations to occur, which results in more excitations per desorbed trajectory. Note that also in the exponential case the desorbed trajectories had more excitations than the average. This indicates that on average there is an energy gain for every of the first few excitation de-excitation cycles. This is further supported by the fact that the average total energy of the desorbed molecules was considerably larger for the Gaussian case than for the other two schemes.

In the figures 4.22 and 4.23 we compare the rotational momentum distribution and the velocity distribution of the three schemes. Note that the distributions are normalised by dividing with the corresponding desorption probability. We see that the distributions for the delta excitation and the exponential scheme are very similar for both the rotation and the velocity, whereas in the Gaussian case the distributions are wider, but with nearly unchanged peak position.

4.8.2 Two Pulse Excitation

After investigating the effect of the shape of the excitation pulse in the previous section we proceeded to simulate two pulse correlation processes. We do so by combining a delta like optical potential at time zero followed by an Gaussian shaped potential

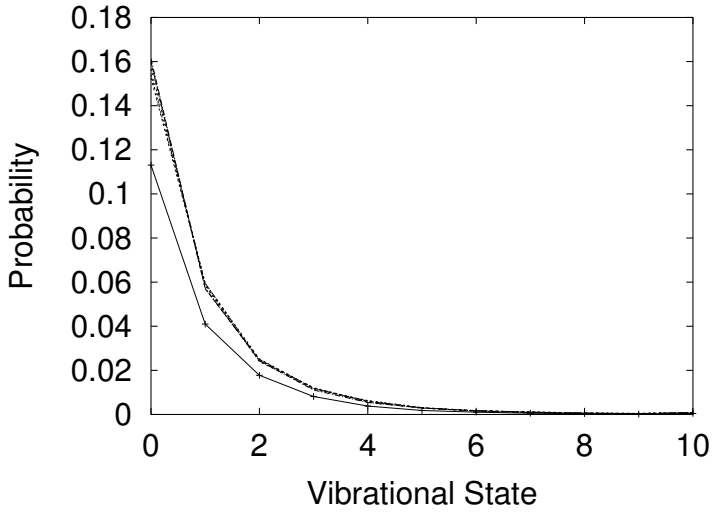

Figure 4.25: The vibrational occupation probability for the different delay times. The lower line with the crosses corresponds to zero delay time, all the other lines lie basically on top of each other and belong to the various larger delay times.

centred at various delay times, where the parameters used for the Gaussian were the same as in the previous section. In figure 4.24 we plotted the desorption probability as a function of the delay time. This plot shows two striking features, first the desorption probability for zero delay time is at 18.6 % basically the sum of the probabilities we get for the separate excitations.

The second notable characteristic is the fact that for all the other delay times the desorption probability is considerably higher and nearly constant, despite a comparable number of excitations per trajectory. Since the width of the Gaussian optical potential is small, compared to the delay times used, the two excitation processes are well separated. We can deduce, that without any energy dissipations, the desorption probability for multiple excitation pulses does not depend on the time between those pulses, as long as they are well separated.

In the experiments the observed behaviour of the molecules desorbing in the vibrational ground state and that of those in a vibrational excited state was different [66]. In the ground state Eichhorn et al. observed an negative correlation at delay-times of 2.5 pico seconds while for all the other states a positive correlation was observed with corelation times of 5-8 ps, see figure 4.2. In figure 4.25 we plotted the vibrational distributions of the desorbed trajectories for different delay times. In contrast with the experimental findings the behaviour is independent of the vibrational state and the same as the desorption probability, lower for zero delay time and constant for all the other delay times.

We showed that, using the same potentials and de-excitation scheme, wave packet results are reproduced well by classical trajectories. By adding a surface oscillator to our model we showed the importance of high dimensional simulations for the theoretical understanding of DIET processes. This also proved the need for a realistic description

of energy dissipation into the surface, in order to avoid dynamical trapping for infinite times.

Chapter 5

Conclusions

We used a mixed quantum classical scheme to investigate the laser induced desorption of NO from small Pd-clusters on alumina support and from the NiO(100) surface. For the first system we used a simple one dimensional model and explored the change of desorption probability with the different parameters of our model. We showed that the experimentally observed changes of the desorption yield, of a factor of ten, could well be reproduced by relatively small parameter changes. The desorption probability does not only depend on the binding energies and the bond geometry but also depends strongly on the excited state lifetime.

For the second system we used ab initio derived two dimensional potential energy surfaces obtained by Thorsten Klüner et al. [2] as the basis of our simulations. By comparing our results with wave packet calculations of the same group [3] we showed that the quantum mechanical results were essentially reproduced by our mixed quantum classical method. In our simulations we found two different species of desorbing NO molecules, early and late ones, where the late desorbing trajectories were neglected in the wave packet calculations. This demonstrated the ability of our method to cover sufficient long propagation times necessary for the correct description of the desorption process. Unfortunately the late desorbing species, which was not included in the wave packet simulations, destroyed the bimodality observed in the initial velocity distributions and in the experiment.

The bimodality could not be recovered by extending the dimensionality of our model. Though it showed the importance of multidimensional simulations, in particular the necessity to include the surface degrees of freedom in the simulation. The desorption dynamics was altered dramatically by the addition of the surface oscillator to our model. The main effect of the oscillator was slowing down the early desorbing molecules and consequently reducing the mean rotational energy to values closer to the experimentally observed rotational temperature. The introduction of a frictional force lead to an suppression of very late desorption, still present with the oscillator, but otherwise had little effect on the momentum distributions.

We can not present a new explanation for the experimentally observed bimodality but the use of spatially confined optical potentials in the de-excitation process might be part of a possible explanation. The bimodality could also be due to different intermediate electronic states being populated during the desorption process.

For the description of the two-pulse correlation experiments a lot of research still needs to be done. However, we showed that in principle our method is capable of describing such reactions. But without a more detailed understanding of the excitation process and a more realistic description of the substrate surface, especially including dissipation, an explanation of the observed correlations seems to be unlikely.

By applying our mixed quantum classical (MQCl) method to the desorption of NO from NiO(100) and small Pd-clusters we hopefully showed the usefulness of such methods for the simulation of DIET processes. We think that MQCl methods can help to identify the relevant coordinates for non adiabatic reactions, since additional degrees of freedom can be included easily. Classical trajectories usually also provide a more intuitive picture of the basic dynamics than wave packages and thus can help in our understanding [72]. Still the foundation of DIET reactions is quantum mechanics and thus for very precise results solving the corresponding equations will be necessary and maybe even more efficient than MQCl, since no statistical sampling is necessary. However, any simulation of the non adiabatic dynamics of nuclei will depend on the correct evaluation of the corresponding electronic states involved and the couplings between them. Unless significant progress is made in calculating electronic excited states this will be the limiting factor of such simulations. Nevertheless we hope that could make a small contribution towards the understanding of the dynamics of surface reactions.

Appendix A

Computer resources

All the simulations presented in this work were done on the computers of T30g, mainly PC's with AMD Athlon XP CPU's running under SuSE Linux and some Compaq Alpha-Workstations with the Alpha version of the SuSE distribution. For the numerical integrations we used the *lsoda* routine from the opdepack library from Netlib (www.netlib.org). This program was written by A. C. Hindmarsh and L. R. Petzold [73, 74]. This routine automatically chooses either a multi-step Adams-Bashforth-Moulton predictor corrector method for no-stiff problems or a backward difference formula (BDF) if the problem is stiff. In our case the problems are no-stiff and the Adams-Bashforth-Moulton method is used. We also compared the *lsoda* routine against other integration methods such as the Bulirsch-Stoer method [75, 76] and found it competitive.

Bibliography

[1] D. S. Sholl and J. C. Tully. A generalized surface hopping method. *J. Chem. Phys.*, 109(18):7702–7710, 1998.

[2] T. Klüner, H.-J. Freund, J. Freitag, and V. Staemmler. Laser–induced desorption of NO from NiO(100): *Ab initio* calculations of potential surfaces for intermediate excited states. *J. Chem. Phys.*, 104(24):10030–10040, June 1996.

[3] T. Klüner, H.-J. Freund, V. Staemmler, and R. Kosloff. Theoretical investigation of laser induced desorption of small molecules from oxide surfaces: a first principles study. *Phys. Rev. Lett.*, 80(23):5208–5211, June 1998.

[4] N. H. Tolk, M. M. Traum, J. C. Tully, and T. E. Madey, editors. *Desorption induced by Electronic Transitions DIET I*, volume 24 of *Springer Series in Chemical Physics*, 1983. Springer.

[5] W. Brenig and D. Menzel, editors. *Desorption Induced by Electronic Transitions DIET II*, volume 4 of *Springer Series in Surface Sciences*, 1984. Springer.

[6] F. M. Zimmermann and W. Ho. State resolved studies of photochemical dynamics at surfaces. *Surf. Sci. Rep.*, 22:127–247, 1995.

[7] G. Eichhorn, M. Richter, K. Al-Shamery, and H. Zacharias. Femtosecond ultraviolet laser-induced desorption of NO from NiO(100)/Ni(100). *J. Chem. Phys.*, 111 (1):386–397, 1999.

[8] M. Bonn, A. W. Kleyn, and G. J. Kroes. Real time chemical dynamics at surfaces. *Surf. Sci.*, 500:475, 2002.

[9] M. Bonn, S. Funk, C. Hess, D. N. Denzler, C. Stampfl, M. Scheffler, M. Wolf, and G. Ertl. Phonon- versus electron-mediated desorption and oxidation of CO on Ru(0001). *Science*, 285:1042, 1999.

[10] H. Petek, M. J. Weida, H. Nagano, and S. Ogawa. Real-time observation of adsorbate atom motion above a metal surface. *Science*, 288:1402, 2000.

[11] W. Brenig, T. Brunner, A. Groß, and R. Russ. Numerically stable solution of coupled channel equations : the local reflection matrix. *Zeitschrift für Physik B*, 93:91–101, 1993.

[12] Axel Groß. Reactions at surfaces studied by ab initio dynamics calculations. *Surf. Sci. Rep.*, 32:291, 1998.

[13] Geert-Jan Kroes. Six-dimensional quantum dynamics of dissociative chemisorption of H_2 on metal surfaces. *Prog. Surf. Sci.*, 60:1–85, 1999.

[14] Axel Groß. The virtual chemistry lab for reactions at surfaces: Is it possible? Will it be helpful? *Surf. Sci.*, 500:347, 2002.

[15] Moritz Hilf. Hochdimensionale Adsorptions- und Desorptionsdynamik von Wasserstoff auf Silizium. Dissertation, April 2000.

[16] Hua Guo, Peter Saalfrank, and Tamar Seidman. Theory of photoinduced surface reactions of admolecules. *Prog. Surf. Sci.*, 62:239–305, 1999.

[17] C. Bach and A. Groß. Semiclassical treatment of reactions at surfaces with electronic transitions. *Faraday Diss.*, 117:99, 2000.

[18] C. Bach and A. Groß. Semiclassical treatment of charge transfer in molecule-surface scattering. *J. Chem. Phys.*, 114:6396, 2001.

[19] John C. Tully. Molecular dynamics with electronic transitions. *J. Chem. Phys.*, 93(2):1061–1071, July 1990.

[20] M. Kampling, K. Al-Shamery, H.-J. Freund, M. Wilde K. Fukutani, and Y. Murata. Surface photochemistry on confined systems: UV-laser-induced photodesorption of NO from Pd-nanostructures on Al_2O_3. *PCCP*, 2002.

[21] E. Pijper, G. J. Kroes, R. A. Olsen, and E. J. Baerends. Reactive and diffractive scattering of H_2 from Pt(111) studied using six-dimensional wave packet method. *JCP*, 2002.

[22] W. Brenig and M. Hilf. Reaction dynamics of H_2 and D_2 on Si(100) and Si(111). *J.Phys.: Condens. Mat.*, 2001.

[23] A. Dianat and A. Groß. High-dimensional quantum dynamical study of the dissociation of H_2 on Pd(110). *subm. to J. Chem. Phys.*, 2003.

[24] P. Hohenberg and W. Kohn. Inhomogeneous electron gas. *Physical Review*, 1964.

[25] W. Kohn and L. J. Sham. Self-consistent equations including exchange and correlation effects. *Physical Review*, 1965.

[26] Sönke Lorenz. *Reactions on Surfaces with Neural Networks.* PhD thesis, Technische Universität Berlin, 2001.

[27] Dietrich Menzel and Robert Gomer. Desorption from metal surfaces by low–energy electrons. *J. Chem. Phys.*, 41(11):3311–3328, December 1964.

[28] P. A. Redhead. Interaction of slow electrons with chemisorbed oxygen. *Can. J. Phys.*, 42:886, 1964.

[29] P. R. Antoniewicz. Model for electron-stimulated and photon-stimulated desorption. *Phys. Rev. B*, 21:3811, 1980.

[30] R. Gomer. Mechanisms of electron-stimulated desorption. In Tolk et al. [4], pages 40–52.

[31] W. Brenig. Quantum theory of electron stimulated desorption. *Z. Phys. B*, 23: 361–368, 1976.

[32] A. Groß and M. Scheffler. Role of zero-point effects in catalytic reactions involving hydrogen. *J. Vac. Sci. Technol. A*, 15:1624, 1997.

[33] C. Crespos, H. F. Busnengo, W. Dong, and A. Salin. Analysis of H_2 dissociation dynamics on the Pd(111) surface. *J. Chem. Phys.*, 114:10954, 2001.

[34] Sharon Hammes-Schiffer and John C. Tully. Proton transfer in solution: Molecular dynamics with quantum transitions. *J. Chem. Phys.*, 101(6):4657–4667, September 1994.

[35] Sharon Hammes-Schiffer and John Morelli. Surface hopping and fully quantum dynamical wave packet propagation on multiple coupled adiabatic potential surfaces for proton transfer reactions. *Chem. Phys. Lett.*, 269:161–170, April 1997.

[36] J. C. Tully. *Modern Methods for Multidimensional Dynamics Computation in Chemistry*, chapter 2. World Scientific, 1998.

[37] John C. Tully. Mixed quantum-classical dynamics. In *Faraday Discussion*, volume 110, pages 407–419, 1998.

[38] R. B. Gerber, V. Buch, and M. A. Ratner. Time-dependent self-consistent field approximation for intramolecular energy transfer. I. formulation and application to dissociation of van der waals molecules. *JCP*, 1982.

[39] D. Bohm. A suggested interpretation of the quantum theory in terms of "hidden" variables. i. *Physical Review*, 85(2):166–179, 1952.

[40] R. P. Feynman. Forces in molecules. *Physical Review*, 56:340–343, August 1939.

[41] John C. Tullt and Richard K. Preston. Trajectory surface hopping approach to nonadiabatic molecular collisions: The reaction of H^+ with D_2. *J. Chem. Phys.*, 55(2):562–572, July 1971.

[42] Michael F. Herman. Nonadiabatic semiclassical scattering. I. analysis of generalized surface hopping procedures. *J. Chem. Phys.*, 81(2):754–763, July 1983.

[43] Michael F. Herman. Nonadiabatic semiclassical scattering. II. solution of two-dimensional models and comparison with quantum results. *J. Chem. Phys.*, 81 (2):764–774, July 1983.

[44] Michael F. Herman. Nonadiabatic semiclassical scattering. III. time dependent surface hopping formalism. *J. Chem. Phys.*, 82(8):3666–3673, April 1985.

[45] Phillip Pechukas. Time-dependent semiclassical scattering theory I. *Phys. Rev.*, 181(1):166–174, May 1969.

[46] Phillip Pechukas. Time-dependent semiclassical scattering theory II. *Phys. Rev.*, 181(1):174–185, May 1969.

[47] Michael F. Herman. Generalization of the geometric optical series approach for nonadiabatic scattering problems. *J. Chem. Phys.*, 76(6):2949–2958, March 1982.

[48] Uwe Müller and Gerhard Stock. Surface-hopping modeling of photoinduced relaxation dynamics on coupled potential-energy surfaces. *J. Chem. Phys.*, 107(16): 6230–6245, October 1997.

[49] D.F Coker and L. Xiao. Methods for molecular dynamics with nonadiabatic transitions. *J. Chem. Phys.*, 102(1):496–510, January 1995.

[50] P. Saalfrank, R. Baer, and R. Kosloff. Density matrix description of laser-induced hot electron mediated photodesorption of NO from Pt(111). *CPLet*, 1994.

[51] Peter Saalfrank. Photodesorption of neutrals from metal surfaces: a wave packet

study. *Chem. Phys.*, 193:119–139, 1995.

[52] R. G. Newton. *Scattering Theory of Waves and Particles*. McGraw-Hill, 1966.

[53] R. Brako and D. M. Newns. Theory of electronic processes in atom scattering from surfaces. *Rep. Prog. Phys.*, 52:655, 1989.

[54] E. Wigner. On the quantum correction for thermodynamic equilibrium. *Phys. Rev.*, 1932.

[55] Franz Schwabl. *Quantenmechanik*. Springer-Verlag, 1993.

[56] Gerhard Herzberg. *Spectra of Diatomic Molecules*, volume 1 of *Molecular Spectra and Molecular Structure*. D. van Nostrand Company, 1950.

[57] Thomas Brunner. *Streuung von Atomen und Molekülen an Oberflächen*. PhD thesis, Technische Universität München, 1990.

[58] Leon Trilling. The interaction of monatomic inert gas molecules with a continuous elastic solid. *SSc*, 1970.

[59] A. R. Burns, E. B. Stechel, and D. R. Jennison. Desorption by electronically stimulated adsorbate rotations. *PRevL*, 1987.

[60] I Kinoshita, A. Misu, and T. Munakata. Electronic excited state of NO adsorbed on Cu(111): A two-photon photoemission study. *JCP*, 1995.

[61] Th. Mull, B. Baumeister, M. Menges, H.-J. Freund, D.Weide, C. Fischer, and P. Andersen. Bimodal velocity distribution after ultraviolet-laser-induced desorption of NO from oxide surfaces. experiments and results of model calculations. *J. Chem. Phys.*, 96(9):7108–7116, May 1992.

[62] T. Klüner, H.-J. Freund, J. Freitag, and V. Staemmler. Laser induced desorption of NO from NiO(100): Characterization of potential energy surfaces of excited states. *J. Mol. Catal. A*, 119:155, 1997.

[63] H. Kuhlenbeck, G. Odörfer, R. Jaeger, G. Illing, M. Menges, Th. Mull, H.-J. Freund, M. Pöhlchen, V. Staemmler, S. Witzel, C. Scharfschwerdt K. Wennemann, T. Liedtke, and M. Neumann. Molecular adsorption on oxid surfaces: Electronic structure and orientation of NO on NiO(100)/Ni(100) and on NiO(100) as determined from electron spectroscopies and *ab initio* cluster claculations. *Physical Review B*, 43(3):1969–1986, 1991.

[64] M. Menges, B. Baumeister, K. Al-Shamery, H.-J. Freund, C. Fischer, and P. Andresen. Dynamical studies of uv-laser-induced NO-desorption from the polar NiO(111) versus the nonpolar NiO(100) surfaces. *JCP*, 1994.

[65] G. Eichhorn, M. Richter, K. Al-Shamery, and H. Zacharias. Vibrational population in femtosecond UV laser desorption of NO from NiO(100). *Surf. Sci.*, 368:67–70, 1996.

[66] G. Eichhorn, M. Richter, K. Al-Shamery, and H. Zacharias. Time-correlated laser desorption of NO from NiO(100)/Ni(100). *Chem. Phys. Lett.*, 289:367–372, 1998.

[67] Thorsten Klüner. *Theoretische Beschreibung der laserinduzierten Desorption kleiner Moleküle von idealen Metalloxidoberflächen*. PhD thesis, Ruhr-Universität Bochum, 1997.

[68] T. Klüner, S. Thiel, H.-J. Freund, and V. Staemmler. The vibrational excitation

of NO desorbing from NiO(100) after UV laser irradiation: is NO^- a possible intermediate species? *Chem. Phys. Lett.*, 294:413–418, 1998.

[69] A. Groß and W. Brenig. Vibrational excitation in the scattering from an almost rigid surface: NO/diamond(110). *Surf. Sci.*, 302:403–409, 1994.

[70] K. S. Upadhyaya, G. K. Upadhyaya, and A. N. Pandey. Unified study of lattice dynamics of NiO. *J. Phys. Chem. Solids*, 63:127–133, 2002.

[71] J. W. Gadzuk. Resonance-assisted, hot-electron-induced desorption. *Surf. Sci.*, 342:345–358, 1995.

[72] Axel Groß, Steffen Wilke, and Matthias Scheffler. Six-Dimensional Quantum Dynamics of Adsorption and Desorption of H_2 at PD(100): Steering and Steric Effects. *Phys. Rev. Lett.*, 75(14):2718–2721, October 1995.

[73] L. R. Petzold. Automatic selection of methods for solving stiff and nonstiff systems of ordinary differential equations. *Siam J. Sci. Stat. Comput.*, 1983.

[74] A. C. Hindmarsh. Odepack, a systematized collection of ode solvers. In R. S. Stepleman, editor, *Scientific Computing*. North-Holland, 1983.

[75] J. Stoer and R. Bulirsch. *Introduction to Numerical Analysis*. Springer, 1993.

[76] W. H. Press, B. P. Flannery, S. A. Teukolsky, and W. T. Vetterling. *Numerical Recipies*. Cambridge University Press, 1986.

List of Publications

1. Christian Bach, Thorsten Klüner and Axel Groß. Simultaion of laser-induced desorption of NO from NiO(100) *Chem. Phys. Lett.*, 376,424-431, 2003.

2. Christian Bach, Thorsten Klüner and Axel Groß. Multi-dimensional mixed quantum-classical description of the laser-induced desorption of molecules *Appl. Phys. A*, 78,231–238, 2004.